

Radiative effects of global MODIS cloud regimes

By

Lazaros Oreopoulos¹, Nayeong Cho^{2,1}, Dongmin Lee^{3,1}, and Seiji Kato⁴

1. NASA-GSFC, Earth Science Division, Greenbelt MD 20771 USA

2. USRA, Columbia, MD 21044 USA

3. Morgan State University, Baltimore MD 21251 USA

4. NASA-Langley Research Center

Revised for the Journal of Geophysical Research Atmospheres

February 2016

Key points:

- (1) Cloud systems can be organized into cloud regimes
- (2) The regimes can be identified from passive observations such as MODIS
- (3) The regimes have very different radiative effects that can be intercompared

Corresponding Author Info:

Lazaros Oreopoulos
Earth Science Division, Code 613
NASA-GSFC
Greenbelt MD 20771
USA
e-mail: Lazaros.Oreopoulos@nasa.gov
phone: +1 301-614-6128

1
2
3
4
5
6
7
8
9
10
11
12
13
14
15
16
17
18
19
20

Abstract

We update previously published MODIS global cloud regimes (CRs) using the latest MODIS cloud retrievals in the Collection 6 dataset. We implement a slightly different derivation method, investigate the composition of the regimes, and then proceed to examine several aspects of CR radiative appearance with the aid of various radiative flux datasets. Our results clearly show the CRs are radiatively distinct in terms of shortwave, longwave and their combined (total) cloud radiative effect. We show that we can clearly distinguish regimes based on whether they radiatively cool or warm the atmosphere, and thanks to radiative heating profiles to discern the vertical distribution of cooling and warming. Terra and Aqua comparisons provide information about the degree to which morning and afternoon occurrences of regimes affect the symmetry of CR radiative contribution. We examine how the radiative discrepancies among multiple irradiance datasets suffering from imperfect spatiotemporal matching depend on CR, and whether they are therefore related to the complexity of cloud structure, its interpretation by different observational systems, and its subsequent representation in radiative transfer calculations.

1 **1. Introduction**

2 A number of recent studies [*Rossow et al.* 2005; *Oreopoulos and Rossow* 2011;
3 *Tselioudis et al.* 2013] have maintained that cloud information does not have to be
4 organized along traditional “cloud type” lines, but rather that a description in terms of
5 dominant mixtures of cloud types, known as “weather states” or “cloud regimes” is more
6 fitting in a variety of contexts. One of the rationales behind the cloud regime concept is
7 that traditional cloud types rarely occur in isolation in a large area $O(100\text{km})^2$ over
8 several hours. Perhaps a dominant cloud type indeed exists, but other cloud types are
9 frequently also present.

10 But how can cloud regimes be identified and defined? Passive observations often
11 used for cloud retrievals have generally good spatial coverage, so the co-occurrence of
12 different cloud types in a wide geographical region can be tackled adequately, as long as
13 clouds are restricted to well-defined continuous layers. Multiple cloud types that overlap
14 can be better identified (subject to different limitations, of course) with active
15 observations, such as those from cloud radars and lidars. But measurements from these
16 instruments suffer from limited spatial coverage. Passive observations have therefore
17 been the more popular choice for compressing information about meso-scale cloud
18 organization into regimes. The existing cloud regime literature has demonstrated that the
19 concept makes sense for decomposing and differentiating among water and energy flux
20 strengths and contributions of prevailing cloud formations [*Oreopoulos and Rossow*
21 2011; *Haynes et al.* 2013; *Lee et al.* 2013; *Oreopoulos et al.* 2014]. Furthermore, cloud
22 regimes are more resistant to the intrusion of small random or statistically insignificant
23 cloud property variations that confuse the interpretation of interannual variability since

the morphology of the full range of cloud optical properties is being accounted for [Tselioudis et al. 2010; Tan et al. 2015]. But these are only some of the types of studies where regimes are considered a suitable framework; more examples of possible applications are given in the concluding section of *Rossow et al.* [2005].

This paper revisits and revises an investigation that has been attempted previously as part of work with broader goals [*Oreopoulos et al.* 2014], namely the study of the radiative effects and radiative importance of MODIS cloud regimes. As will hopefully become apparent from what follows, the availability of new datasets makes a return to this topic worthwhile. New analysis angles reveal less explored hitherto radiative features, such as flux profiles decomposed by CR. Use of different data sources for radiative flux information, allows intercomparisons organized in ways not shown before.

The presentation of the new CRs takes a big part of section 2, which also documents the various datasets and methodology of use, and extends to section 3 as well. The three subsections of section 4 contain the outcomes of compositing three different radiative flux datasets and comparisons among them where feasible and appropriate. In the concluding section 5 we find fitting to offer thoughts on lessons learned from the analysis, how the findings can be used for related problems, and what new avenues of investigation may be worth pursuing.

2. CR derivation and datasets

a) Cloud Regimes

The core dataset required to derive the revised MODIS cloud regimes is daily $1^\circ \times 1^\circ$ gridded joint histograms of cloud optical thickness (τ) and cloud top pressure (p_c). We

47 use 12 years (December 1, 2002 to November 30, 2014) of such data from both the Terra
48 and Aqua satellites. The most recent version of this dataset used here known as
49 “Collection 6” (C6, henceforth) provides two major options on what type of joint
50 histograms to use: one with and one without so-called “partially-cloudy” (PCL) pixels
51 [Zhang and Platnick 2011; Pincus *et al.* 2012] included. In practical terms the choice
52 amounts to whether to account only for pixels surviving so-called “clear-sky restoral”
53 [King *et al.* 2006; Zhang and Platnick 2011] or to use all cloudy pixels for which an
54 optical property retrieval was successful, even if those were edge pixels. The reason edge
55 pixels are flagged separately as candidates for exclusion is that they are even less
56 appropriate than interior cloud pixels to be treated by the plane-parallel radiative transfer
57 model used to interpret the observed reflectances in terms of cloud optical properties of
58 uniform pixels. We opted for using the version of the histograms that includes PCL
59 pixels, motivated to some extent by the desire to match more closely climatological cloud
60 fractions in the ISCCP dataset. Such a histogram is not directly available, but can be
61 obtained by summing two types of C6 joint histograms, one without the PCL pixels and
62 one that includes only the PCL pixels. The latter histograms were not available in
63 MODIS C5.1, so the MODIS global CRs of Oreopoulos *et al.* [2014] (O14, hereafter)
64 were derived with no PCL pixels accounted for, a factor that probably contributes
65 substantially to the differences between those CRs and the ones here. With the joint
66 histograms being available only during daytime (since reflected solar radiation is needed
67 to derive τ), the CRs obtained according to the procedure described below represent
68 strictly daytime only cloud organizational structures. Of course, the joint histograms
69 include the consequences of limitations in passive observations such as the inability to

properly identify cloud layers obscured by clouds above, misinterpretations of some multi-layer cloud scenes, and occasional strong contributions to the satellite signal by certain highly reflective surfaces. In specific areas of the globe cloud property retrieval errors also occur because of strong aerosol presence either above (e.g. off the west coast of Africa) or between (e.g., East Asia) clouds.

The methodology used to derive the MODIS C6 global CRs is similar to that implemented by O14, but with an important modification. The *k*-means clustering method [Anderberg 1973] used in O14 as well as in the derivation of the ISCCP weather states [Jakob and Tselioudis 2003; Rossow *et al.* 2005; Tselioudis *et al.* 2013) is employed again, but we found empirically that more physical and robust results can be obtained by starting with a small number of baseline or “core” CRs and then breaking these further into “sub-regimes” as in Mason *et al.* [2014]. The number of initial core regimes and the subregimes into which each may be optimally broken was determined by numerous trials that tested the extent to which the criteria of Rossow *et al.* [2005] were satisfied. We settled into six core regimes, and then examined whether each should be further broken into two or three subregimes or whether breakdown into subregimes was not needed. The basic criterion used in deciding whether a core regime should be broken into two or three subregimes (or remain intact) was whether the resulting subregimes differed enough from the original regime and amongst themselves. Differences were quantified in terms of spatial pattern correlation coefficients between the centroids (i.e., mean joint histograms) that define a regime or subregime and the maps of their geographical occurrence expressed in terms of Relative Frequency of Occurrence (RFO), as defined in the papers referenced above. If both correlations were above, somewhat

arbitrary, subjectively-set values (0.6 for centroid patterns; 0.8 for maps), then it was deemed that the subregimes were not different “enough”. At the outset, each regime was broken into three subregimes. If at least two out of three subregimes were similar, the next iteration consisted of only two subregimes. If these two (sub)regimes were again too similar, then only the original core regime was retained, i.e., a breakdown into subregimes was not appropriate. The physical meaning of the latter situation is that the joint histograms belonging to a CR are too similar to be grouped further into distinct subgroups. An additional factor that was taken into account was whether the process of breaking into subregimes resulted in the same outcome regardless of the (random) initialization of the clustering algorithm. If a large majority of the trials gave the same result, then the subregime determination process was considered robust. We found in practice that with only two or three subregimes being possible outcomes, repeatability of results was not an issue. Note that the same criterion of insensitivity to algorithm initialization was also applied to the initial core regimes.

The end result of the above procedure was twelve (12) CRs when all MODIS C6 Terra and Aqua data treated as a single ensemble. These twelve regimes resulted as follows: Four “core” regimes were broken into two subregimes each, one regime was broken into three subregimes, and one regime remained intact (i.e., no subregimes satisfied our criteria in the latter case). Upon completion of the CR derivation procedure, no distinction is retained between regimes that were originally core regimes and regimes that descended from a core regime through subregime clustering, i.e., all are considered CRs of equal stature. The CR pairs and triplet that have a common core CR progenitor are: CR2 and CR3; CR4 and CR5; CR7 and CR8; CR10 and CR11; CR1, CR6 and

CR12. CR9 is the only regime that did not come from a split. Gridcell RFOs come from normalization relative to the total number of regime occurrences in that gridcell, and global RFOs are area-weighted averages (by cosine of latitude) of gridcell RFOs. The CR indices are assigned based on the location of cloud fraction local maxima within the CR centroid, so that CRs with peak cloud fractions at higher altitudes are assigned smaller indices.

The CR centroids are shown in Fig. 1, with corresponding geographical distribution of RFO in Fig. 2. The RFO and CF values for each CR in Fig. 1 as well as the maps of Fig. 2 correspond to multi-annual means. Tables 1 and 3 in the supplementary material provide multi-year seasonal means and separate annual means for Terra and Aqua, respectively.

Joint inspection of Figs. 1 and 2 provides a fairly unambiguous picture of the cloud mixtures represented by the twelve MODIS C6 global CRs. A basic initial description is provided below, while further insight is provided in section 3 aided by additional data.

The regime with the largest proportion of high clouds, many of them of small optical thickness, is CR1 and appears to contain a lot of the tropical cirrus associated with convection, but also deeper clouds; it is arguably the most tropical of all CRs with a pronounced presence in the Pacific ocean, and elsewhere within the confines of ITCZ. CR2 contains most of the optically thickest clouds of all regimes, especially those reaching high altitudes; it appears to comprise the strongest storm systems produced by tropical and frontal convection and has the highest cloud fraction (CF) of all regimes. Closely associated with CR2 is apparently CR3 which tracks tightly the geographical pattern of CR2, but evidently contains the thinner elements of storm activity (in cyclonic

139 parlance one would say that it represents cyclone sectors that are different from those
140 usually contained in CR2); presence over both land and ocean can be seen. The next two
141 regimes CR4 and CR5 appear to also be closely associated with very alike geographical
142 patterns of RFO. Bin CF peaks within the same pressure bin, but CR4 has more of the
143 optically thicker clouds and overall greater CF. These two regimes are almost exclusively
144 extratropical and are apparently dominated by alto- and nimbo- type clouds in higher
145 latitude (except for the Tibetan peak) storm systems. A closer look has shown that CR4 is
146 more prevalent during the summer months and CR5 during the winter months of the
147 respective hemisphere. CR6 is the closest of our regime set fitting the characterization of
148 a mid-level CR, and exhibits strong presence over land areas with the exception of the
149 near-polar southern latitudes and the Pacific segment of the ITCZ where it may contain
150 congestus type clouds. The next five regimes represent cloud mixtures where various
151 types of shallow and boundary layer clouds are dominant. Among this group, CR7 has
152 the optically thickest clouds and the largest CF, but also the smallest RFO (as a matter of
153 fact, the smallest RFO of all CRs); it is mainly a high latitude CR of plentiful thick stratus
154 over both lands and oceans. CR8 has occurrence peaks in known marine stratocumulus
155 areas, but also occurs in far south oceans and over northern lands. A more pure marine
156 profile characterizes CR9 which also makes a strong presence in marine stratocumulus
157 areas; its CF is similar to CR9 but appears to contain clouds that are shallower and less
158 optically thick. CR10 is also mostly marine, but its substantial lower CF compared to
159 CR9 indicates more broken stratocumulus and shallow cumulus. The latter cloud type
160 seems to be even more dominant within CR11, as suggested by small optical thicknesses
161 and low cloud fractions; this particular regime is almost exclusively oceanic with

negligible presence in high latitudes. Finally, CR12 comprises all 2D histograms of small CF with no characteristic shapes to suggest a specific identity. It is the regime with the highest global RFO and smallest CF; CRs of this type emerged not only in O14, but also in the ISCCP version of global CRs derived by *Tselioudis et al.* [2013]. This regime occurs almost everywhere except the nearly always overcast far southern oceans.

Common features, but also differences can be identified when comparing these CRs to those by O14. First, there is no counterpart to CR1 in O14. CR1 in our analysis emerged from the only core CR split into three subregimes. Second, low-level and boundary layer cloud systems with CFs above 65% are resolved in more regimes in this analysis (four here vs. two in O14). Third, the current set of regimes has only one CR with peak cloudiness between 440 and 680 hPa, while in the C5.1 set of O14 there were two; this is consistent with an overall drop of the mid-level cloud population in C6 compared to C5.1. The semi-clear low CF “shapeless” regime of this study (CR12) is more populous with an RFO of ~41%, but has a larger CF (~29%) than its C5.1 counterpart (CF ~20%) occurring about ~31% of the time, probably because of the inclusion of PCL pixels in this study. If one compares, however, the combined global RFO of the two CRs with the lowest CFs (CR11 and CR12 in this study), the numbers are similar: ~53% in this study compared to ~50% in O14.

In summary, the updated regimes now include a new high-cloud regime that did not exist before, no clear-cut mid-cloud regimes, more low-cloud regimes, and a “featureless” regime with higher CF and RFO than its C5.1 predecessor.

b) Other MODIS cloud variables

In addition to the p_c - τ joint histograms we also use other MODIS cloud variables from Level-3 daily 1° gridded data which are composited by CR and are sometimes used only for internal diagnostic and interpretation purposes (one such use was guidance for the subregime analysis). Such variables are liquid and ice CF of successful MODIS retrievals, mean combined τ (also available by cloud thermodynamic phase), and mean p_c . Individual and composite values for all these variables are calculated with PCL pixels accounted for consistency with the joint histograms used in the CR derivation.

c) CERES radiative fluxes

We use two types of SYN1deg Edition 3A CERES radiative fluxes to examine the radiative behavior in terms of the Cloud Radiative Effect (CRE) (defined later) of the new global MODIS CRs. Both products are gridded at 1°, but one is diurnally (24-hour) averaged (SYN1deg-daily) while the other represents 3-hour averages (SYN1deg-3hr). The SYN1deg products use 3-hourly geostationary (GEO) satellite radiances and cloud properties to more accurately model the diurnal variability between CERES (Terra and Aqua) observations. The Top-Of-the-Atmosphere (TOA) fluxes (all-sky and clear-sky) are temporally interpolated from observed fluxes at the time of CERES overpasses using the GEO information [Doelling *et al.* 2013]. Surface (SFC) fluxes come from a broadband radiative transfer code which uses as input MODIS and GEO cloud properties, atmospheric profiles provided by the Goddard Modeling and Assimilation Office (GMAO), and MODIS aerosols [Rutan *et al.* 2015]. Compositing CERES CREs (and all other variables for that matter) by regime essentially amounts to deriving an area-weighted global average from all CRE values that coincide spatiotemporally with a given

regime occurrence. The details of the compositing and the distinctive treatment of the two CERES products will be provided in the appropriate results subsection. The length of the CERES datasets is the same as that of the MODIS CR, i.e., December 1, 2002 to November 30, 2014.

d) CloudSat-CALIPSO-based radiative fluxes

The radiative products from CloudSat and CALIPSO (hereafter often referred to collectively as “CC”) composited as a function of MODIS CR come from the 2B-FLXHR-LIDAR (R04) dataset. This dataset is produced from an algorithm that builds off the predecessor 2B-FLXHR algorithm [L’Ecuyer *et al.* 2008] by taking advantage of recent improvements in cloud and precipitation products and by explicitly accounting for clouds and aerosols not detected by CloudSat itself [Henderson *et al.* 2013]. The unique feature of the dataset is its full profiles of radiative flux coming from radiative transfer calculations applied to vertical profiles of cloud properties retrieved from CC observations [L’Ecuyer *et al.* 2008; Henderson *et al.* 2013]. A clear-sky radiative flux profile is also provided (obtained by a second radiative transfer calculation where cloud is removed while everything else remains the same), which allows thus calculation of CRE profiles. Since the CC duo is part of the A-Train [L’Ecuyer and Jian 2010] of which Aqua is also a member, we composite radiative flux (CRE) profiles for the 1:30 pm CC overpass and only for CR occurrences at that time, i.e., from Aqua. Specifically, we combine (average) all 1:30 pm irradiance profiles that fall into the 1° gridcell that contains a particular Aqua CR occurrence. The flux/CRE profiles are available for both the LW and SW spectral domains. Similar compositing is applied to two CRE variables

provided separately, TOACRE and BOACRE (for top and bottom of the atmosphere, respectively). These two CREs assume slightly different values than those obtained by subtracting clear and all-sky values for the topmost and lowest level (valid) values of the flux profile.

When converting CREs to a measure of cloud impact on heating rates (see eqs. 3 and 4 that follow), atmospheric density profiles are needed. These can be calculated from atmospheric variables provided in the ECMWF-AUX CloudSat product. The ECMWF-AUX dataset is an intermediate product that contains the set of European Center for Medium-Range Weather Forecasts (ECMWF) state variables interpolated to each CloudSat Cloud Profiling Radar (CPR) bin from the ancillary AN-ECMWF analysis dataset.

The time period covered by the 2B-FLXHR-LIDAR and ECMWF-AUX datasets is January 1, 2007 to December 31, 2010 (four years).

e) AIRS radiative fluxes

LW radiative fluxes at the TOA (also known as Outgoing Longwave Radiation – OLR) at the time of the Aqua satellite overpass are likewise available in the AIRS V6 Level-3 dataset also on a 1° grid. These come from radiative transfer calculations that use information from the AIRS/AMSU (Atmospheric InfraRed Sounder/Atmospheric Microwave Sounding Unit) instrument suite [Pagano *et al.* 2003] aboard Aqua (hereafter simply referred to a “AIRS”). Details on how these irradiances are derived can be found in Susskind *et al.* [2012]. In simple terms, AIRS-derived profiles of temperature, humidity, ozone, carbon dioxide, and surface skin temperature, as well as cloud

properties are used as input into the radiative transfer code RRTMG-LW [Iacono *et al.* 2008] which produces irradiances at desired atmospheric levels. A clear-sky flux calculation is also made separately, so CRE can be assessed again the usual way (see eq. 1 that follows). We use only the flux calculation from the 1:30 pm (daytime) Aqua overpass, since CRs are available only during daytime. The time period covered by the AIRS CRE LW dataset is the same as that for the MODIS CRs, i.e., December 1, 2002 to November 30, 2014.

3. Additional insight into the MODIS CRs

The interpretation of the CRs provided in subsection 2a is consistent with the dynamical environment in which CRs are embedded, at least as represented by the large-scale vertical velocity at 500 hPa. This velocity is commonly obtained by re-analysis. Following this established practice we choose MERRA [Rienecker *et al.* 2011] re-analysis data for performing a CR-based compositing of pressure velocity. Fig. 3 shows the outcome of this exercise in the form of a boxplot. The clear pattern seen in the figure supports the choice of the term “weather state” [Rossow *et al.* 2005] for what we call here CR. While our index assignment was blind to the dynamical environment, we see that it is quite effective in organizing regimes in terms of large-scale vertical motion: the first six CRs occur in areas where the mean (and median) vertical velocity indicates ascending motion, while the six CRs assigned the highest indices occur in areas where descending motion at 500 hPa prevails. CR2, containing the thickest and deepest clouds occur in environments of strongest ascent; while the ascent is weaker for CR4 and CR5, these regimes still occur in environments virtually devoid of large-scale descending motions in

the mid-troposphere. For CR7-CR11, regimes with abundant shallow and boundary layer clouds, descending motions dominate. Low CF CR12, containing no clear dominant cloud type and being omnipresent, is similarly ambiguous in terms of its dynamical environment which exhibits near equal amounts of large-scale descent and ascent. Other atmospheric indicators can of course be invoked to describe the environment in which CRs are embedded, even including sophisticated representations within joint dynamical-thermodynamical phase spaces, but we limit ourselves to large-scale vertical motion as a signifier of atmospheric information content implicitly residing in p_c - τ histograms. Simply put, the clustering algorithm applied to such joint variations appears to be quite skillful in deriving meaningful modes of cloud organization.

The CR concept by design encourages dismissal of standard cloud discrimination conventions based often on naïve criteria such as cloud thermodynamic phase. Nonetheless, Fig. 4 shows that our CRs have clear thermodynamic phase traits, with most CRs assuming a predominant (in terms of cloud fraction) liquid or ice phase identity. Only CR4 and CR12 are relatively balanced in terms of their ice and liquid cloud fractions. The first three CRs, not surprisingly given their large proportions of high clouds are dominated by ice phase clouds. CR5, also consists mostly of ice clouds; recall that we identified this CR as the winter doppelgänger of the “summer” CR4 which naturally contains more liquid than ice clouds. CR7-CR11 encompass mostly liquid clouds consistent with centroids exhibiting peaks at high atmospheric pressures (low altitudes). It is less easy to predict the dominant thermodynamic phase of CR6 from the appearance of the centroid alone, but it turns out that it too consists mostly of liquid clouds, at least according to the MODIS phase discrimination algorithm.

A more traditional breakdown of CRs by cloud type is shown in Fig. 5. What is less traditional is the way the proportion of each cloud type was derived and how the cloud types were identified. Specifically, they come from the CloudSat 2B-CLDCLASS dataset, i.e., from a sorting and classification of active CPR observations. We used the form of the dataset aggregated in the merged CERES/CloudSat/CALIPSO/MODIS (CCCM) product [Kato *et al.* 2010; 2011]. A similar breakdown with the same dataset was also shown in O14. Examination of Fig. 5 indicates a general consistency between active (2B-CLDCLASS) and passive (2D MODIS histograms) cloud views. The fraction of *Sc* clouds (given the absence of *St* in meaningful amounts in the 2B-CLDCLASS product) serves as a good indicator of affinity with Fig. 4, as well as the various centroid panels of Fig. 1 (a cloud type abbreviation key is provided in the caption of Fig. 5). CR7-CR11 have the largest fraction of *Sc*, re-affirming their shallow and boundary layer character. CR2, embedded in the strongest large-scale ascent environments has the most *Cb*'s, while CR1 has most *Ci* than any other regime in accordance with what is visually conveyed by its centroid. If the fraction of high- and mid-topped clouds were to be inferred by the sum of *Cb*, *Ci*, *As*, and *Ac* fractions, then the first three CRs are in a category of their own, with about 70% of their composition coming from such clouds. CR4, CR5, and CR6 have the largest fraction of *Ns*. While CR4 and CR5 cannot be discriminated by their combined fraction of *Sc* and *Cu*, CR4's more stormy nature is exposed by more *Ns* and *Cb* clouds. Fig. 5 also confirms that CR12 is hardly a cloud regime with only shallow clouds; as its centroid suggests, high proportions of mid- and high-level clouds are also found, albeit in small absolute numbers since the CF of the regime is so low.

323

324 **4 CR Cloud Radiative Effects**

325 *a) From CERES*

326 For our basic results we largely follow previous choices and practices on how to present
327 CR radiative effects in terms of CRE. The gridcell CRE (for either the LW or SW or part
328 of the spectrum, and for *total*=LW+SW) is defined here as:

$$329 \quad CRE = F_{all-sky} - F_{clr} = A_c(F_{ovc}[f(p_c, \tau)] - F_{clr}) \quad (1)$$

330 where $F_{all-sky}$ is the radiative flux for a mixture of clear and cloudy conditions within the
331 gridcell, F_{ovc} (mainly a function of p_c and τ) is the radiative flux (irradiance) of overcast
332 skies, F_{clr} is the corresponding flux for “clear” (cloudless skies), and A_c is the gridcell
333 cloud fraction (reserved for the gridcell value, as opposed to the physical variable CF).

334 When using the SYN1deg-daily data we composite (i.e., average globally using
335 latitude as weight) only gridcells occupied by the same CR for both Terra and Aqua;
336 these special gridcells represent 25.4% of the total number of gridcells analyzed
337 ($\sim 435.5 \times 10^6$). This approach was discussed in O14 as essentially the best available (but
338 certainly imperfect) criterion for identifying persistence of a particular CR within a
339 gridcell. Except for this condition, the compositing is rather straightforward since both
340 the CR and the CERES SYN1deg-daily dataset are available at the same temporal (one-
341 day) and spatial (one degree) resolution and for an identical time period. Results shown
342 in Figures 6-8 convey three basic results, the position of each CR in SW/LW/*total* TOA
343 CRE space, the percent contribution of each CR to the total SW/LW/*total* planetary TOA
344 CRE, and the contrast between the LW CRE at the TOA and SFC which provides insight

on each CR's average radiative cooling or warming effect on the atmosphere (the trivial SW warming effect across all CRs is not shown). Net fluxes (down F^\downarrow minus up F^\uparrow) are used in Eq. (1) to derive the results shown in these figures. When using net fluxes LW CRE assumes almost always positive values while SW CRE negative values at both TOA and SFC. The information content of these three figures will be discussed in some detail next.

The salient information content of Fig. 6 is the average radiative strength at the time of regime occurrence. CR2 and CR4 stand out, with CR2 having the most pronounced radiative effects of the two in both the LW and SW part of the spectrum. This comes as no surprise given that CR2 has large fractions of clouds that have both high tops and large optical thicknesses. The notable drop of LW CRE from CR2 and CR4 is of course related to cloud populations in CR4 with overall lower cloud-top altitudes. Differences in the SW CRE averages, on the other hand, come from slightly smaller overall optical thicknesses in CR4 and locations of occurrence that receive lower illuminations overall. Incoming solar radiation plays again a big role (in addition to cloud optical thickness and cloud fraction) in the huge difference between the SW CREs of CR4 and CR5 despite maps of (multi-) annual RFO that look very similar. As has been discussed earlier, CR5 is predominantly a winter and CR4 a summer regime. CR7 and CR9 have similar (and quite strong) SW CRE and small LW CRE (higher cloud tops give an edge to CR7) consistent with their perceived image as extensive (in terms of CF) and relatively thick low-level clouds. The next group of CRs roughly consisting of CR1, CR3, CR6, and CR8 have mean SW CREs that are about 20 Wm^{-2} lower (in absolute values), but exhibit an extremely wide range of LW CRE reflecting large differences in cloud top altitudes

prevalent within those regimes. CR10, CR11, and CR12 straddle similar low values of LW CRE due to combinations of low CFs and lack of high clouds in sufficient numbers; CR10 seems to have thicker clouds and greater CF than the other two, and thus separates in terms of SW CRE.

CR12 is the only CR that has near zero net CRE, with all other regimes exhibiting a vast range of negative values and therefore exerting varying degrees of radiative cooling effect on the earth-atmosphere system (note that SW cooling is realized at the surface and LW cooling or warming mainly within the atmosphere). The largest cooling effect does not come from CR2, the regime with the highest individual LW and SW CRE values, but from the low-cloud dominated CR9, followed closely by CR7 and CR4. Even CR1 with its many cirrus clouds has an overall negative net CRE despite positive values occurring in about 47% of the samples used to determine the CR1 mean in this plot.

The global TOA CRE numbers from the special sample used here (gridcells that have the same CR for both Terra and Aqua) are largely consistent with figures published previously [*Harrison et al.* 1990; *Zhang et al.* 2004; *Stephens et al.* 2012; *Henderson et al.* 2013]. Our global SW CRE is -46.2 Wm^{-2} and our LW CRE 26.1 Wm^{-2} , values derived by taking a weighted average of individual CR CRE means, with CR global RFOs serving as weights.

The variability of CRE values is depicted by the horizontal and vertical error bars which represent (one fifth of) the interquartile range of the distribution used to calculate the composite means. The error bars therefore provide guidance on how wide the distribution of CRE values is for each CR, and not on the uncertainty of the means. Seasonal changes in solar illumination contribute greatly, of course, to the SW CRE

variability. But the CRE variability is also a strong function of the dominant CRE magnitudes in the distribution (regimes with small overall CRE such as CR10, CR11, and CR12 have also small interquartile ranges). The only regimes with comparable SW and LW interquartile ranges are CR1 and CR3; of the two, CR1 has also almost equal mean SW and LW CRE values. The low-cloud dominated regimes CR7 and CR9 have very large SW CRE variability, but negligible LW CRE variability.

While Fig. 6 distinguishes radiatively strong and weak regimes at the time of occurrence, what eventually matters from an energetics perspective is a CR's overall radiative contribution which also depends on its frequency of occurrence (RFO). The role of RFO is incorporated in the results of Fig. 7 because the percent contributions of CRE shown in this figure were calculated by dividing the sum of all CRE values corresponding to a CR to the sum of all available CRE values (subject to the sampling strategy for CERES SYN1deg- daily data discussed earlier). In this representation, the radiative contributions of the previously weak CR12 are so large, because of its huge RFO, that a special insert into the plot is required: CR12 contributes about 39% of the global LW CRE and ~24% of the SW; but it has a far less remarkable ~6% contribution to *total* CRE because of its near-zero average *total* TOA CRE. CR1, CR3, and CR5 stand out for their even smaller *total* CRE contributions, even though the first two have quite large SW and LW contributions; this is because they belong to the group of CRs with small average *total* CRE (Fig. 6). CR2, the strongest regime in terms of average CRE, falls fourth when CRE contributions are examined because of its unimpressive RFO. Low-cloud dominated CR9 has the distinction of largest discrepancy between LW and SW CRE contributions: its relative contribution is three times larger in the SW than the LW.

O14 demonstrated a rather unambiguous separation of MODIS C5.1 CRs into those that radiatively warm and those that cool the atmosphere. We have now updated those results in Fig. 8 and again focus on only the LW part of the spectrum since the SW effect is known to be a small nearly universal warming (cloud presence contributes a small additional amount of atmospheric absorption). When the LW CRE at SFC is greater than the LW CRE at TOA clouds have a cooling effect on the atmosphere and vice-versa. With the exception of CR12 which sits on the diagonal of zero atmospheric radiative effect, the regimes separate quite well into radiative warmers and coolers. Those above the diagonal (cooling) have the largest proportions of low clouds, while those below the diagonal (warming) have many high clouds. CR7, CR8 and CR9 are the regimes with the more prominent cooling, while CR1, CR2, CR3 induce the highest radiative warming. The overall result (taking the RFO-weighted average) of 0.75 Wm^{-2} from the sample used here suggests a near balance between cloud-induced cooling and warming, consistent with previous results: *Henderson et al.* [2013] found a slight warming of $\sim 1.5 \text{ Wm}^{-2}$, while the ISCCP-based results of *Zhang et al.* [2004] and our own analysis of CERES EBAF (Energy Balanced And Filled) data indicate a slight cooling of approximately -3 Wm^{-2} . Despite the SW CRE (warming) effect being small, its additive nature (no cancellations as in the LW) brings the cloud global *total* atmospheric CRE to $\sim 3 \text{ Wm}^{-2}$, a value, once again, that is specific to the data sample used here.

Similar to Fig. 6, we include information about the variability of the LW CRE values in terms of interquartile range values (1/2 of the actual value is shown for clarity). The CRs below the diagonal with CRE at TOA greater than at the SFC tend to also exhibit greater variability in TOA CRE; the opposite happens for the CRs above the

diagonal. An extreme example of strong TOA CRE variability and almost no SFC CRE variability is CR1 which occurs largely in the tropics where the LW effect of clouds at the surface is small and barely variable given how strongly the downwelling LW flux is modulated by near-surface atmospheric temperatures in very humid environments.

The SYN1deg-3hr dataset offers the means to examine radiative impacts of Terra and Aqua CR occurrences separately. Basically, a similar analysis as with the SYN1deg daily dataset can be conducted, but with matching in this case a Terra or Aqua CR occurrence with the 3-hr average CERES flux of the same gridcell that contains the appropriate daytime satellite overpass. We compare Terra and Aqua CRE breakdown in Fig. 9: the top two panels show the magnitudes of SW and LW CRE while the bottom two panels show the percent contributions to the global Terra and Aqua CRE. A SW CRE magnitude comparison is apt because of insolation symmetry around local noon (subject, of course, to the coarse 3-hour temporal resolution of the CERES dataset).

CR2, the regime with the largest mean values of LW and SW CRE is also the regime with the largest Terra-Aqua discrepancy. This is not the case for contributions, where CR2 ranks lower. Both in terms of absolute magnitudes and contributions, the Aqua value is larger, consistent with the expectation of stronger convection during afternoon hours. In general Aqua LW CRE is greater for regimes CR2 to CR5, all in the top-5 of strongest LW CREs. Interestingly, SW CRE is not as distinct between Terra and Aqua for CR3 and CR5 (although contributions for these regimes are bigger for Aqua); this makes it less likely that morning-afternoon differences in LW CRE come from CF changes (a conclusion confirmed by Supplementary Material Table 3 which shows small CF differences on an annual basis). The regimes with cloud populations consisting

mainly of low clouds show almost no differences in (already low) LW CRE, but three of them, CR7, CR8, CR9 exhibit notable differences in SW CRE. For CR9, the difference in the magnitudes themselves translates to almost no contribution difference; for the other two regimes, however, larger Aqua SW CRE means are apparently not enough to translate to bigger relative contributions to the Aqua global CRE; the importance of these regimes is therefore bigger for the Terra global SW CRE. In general, when comparing regimes in terms of relative CRE strengths, we see consistency between the LW and SW parts of the spectrum, in the sense that regimes with bigger contribution imprints for Terra compared to Aqua maintain that feature for both parts of the spectrum: CR2, CR3, CR4, CR5 matter more in the afternoon for both LW and SW CRE, while CR1, CR7, CR8, and CR12 matter more in the morning (for all other regimes differences are less noteworthy).

b) From CloudSat-CALIPSO

Despite being based on more spatially limited observations and providing imperfect areal matching with our other radiation datasets, the 2B-FLXHR-LIDAR product [L'Ecuier *et al.* 2008; Henderson *et al.* 2013] which comes from application of radiative transfer calculations on cloud retrievals from active CC observations, enables an enriched perspective on the radiative effects of CRs. Specifically, this dataset allows examination of regime radiative impacts throughout the depth of the atmosphere either in terms of CRE or as cloud effects on the atmospheric heating/cooling rates of atmospheric layers. A measure of the latter is the difference between all-sky and clear-sky heating/cooling rates called here Cloud Radiative Heating (*CRH*) following Haynes *et al.* [2013]:

$$CRH = \left(\frac{dT}{dt}\right)_{all-sky} - \left(\frac{dT}{dt}\right)_{clr} \quad (2)$$

where

$$\frac{dT}{dt} = -\frac{1}{\rho C_p} \frac{dF}{dz} \approx -\frac{1}{\rho C_p} \frac{[(F^\downarrow(z) - F^\uparrow(z)) - (F^\downarrow(z+\Delta z) - F^\uparrow(z+\Delta z))]}{\Delta z} \quad (3)$$

so that

$$CRH = -\frac{1}{\rho C_p} \frac{dCRE}{dz} \approx -\frac{1}{\rho C_p} \frac{CRE(z) - CRE(z+\Delta z)}{\Delta z} \quad (4)$$

T , ρ (from ECMWF-AUX), C_p , z , t , are the air temperature, air density, specific heat of dry air under constant pressure, altitude, and time. With an appropriate scaling factor, CRH can be expressed in units of K/day. Note that the reliability of CRH is somewhat tarnished by the nature of the calculation where eight distinct fluxes (four clear and four cloudy at the layer boundaries) are used.

We first look at CRE profiles partitioned by CR. The plots show profiles of CRE for upward, downward as well as net (down minus up) flux separately for the LW (Fig. 10) and SW (Fig. 11) part of the spectrum. The profiles were calculated by averaging the valid flux values belonging to a CR for each of the 125 vertical layers followed by height assignment for each layer by taking the mean of all heights corresponding to that layer (because the height of a layer differs by location). Given the definition of CRE by eq. (1), the profile of LW CRE retains negative values for upward flux, and positive values for downward and net fluxes. The opposite occurs for SW: upward CRE is positive, while downward and net CRE assume negative values. Because the downward LW CRE is zero at TOA and so is the upward LW CRE at SFC, the net LW CRE equals the upward CRE at TOA (in absolute values) and the downward CRE at the SFC. Virtually opposite behavior is seen for the SW, the only difference being that the upward SW CRE at the

SFC is slightly different from zero because of different SFC upwelling flux under clear and cloudy skies; the end result is that the downward and net SW CRE at the SFC are not exactly identical, while the upward SW CRE at TOA matches exactly the net CRE in absolute values.

The CRE plots for LW are probably more intriguing than those for SW. The LW profiles exhibit progressively less structure as one moves from low to high index CRs. The main guiding principle to keep in mind when examining these plots is that a value at a particular level in the upward CRE profile represents the cumulative effects of all clouds below, while for the downward CRE profile it represents the cumulative effect of the clouds above. The shape of the upward and downward CRE profiles therefore reflects the configuration of the vertical locations of cloudiness within each CR, with the more prominent features associated with locations of peak cloudiness. One difference between the two profiles is that the upward CRE profile is monotonic, i.e., values increase in an absolute sense from SFC towards TOA; the downward CRE profile on the other hand exhibits a peak at some level within the atmospheric column. The former behavior can be explained by the larger opacity of cloudy compared to clear skies and the fact that average tropospheric temperature drops with altitude: as one moves upward the contrast between clear and cloudy sky in terms of the cumulative effects of the atmospheric layers below always increases (i.e., the radiative emission height of cloudy skies moves more rapidly upwards, toward colder temperatures, than in clear skies, given that cloudy opacity grows faster than clear sky opacity) widening thus the contrast between clear and cloudy flux. In the case of the downward flux the LW CRE will inexorably start to decrease towards lower altitudes at some height as the contrast in downward cumulative

opacity (which moves the emission height for downward flux to lower levels) is compensated by temperature increases towards lower altitudes. In other words the distance between clear-sky and cloud-sky emission height after reaching a peak, decreases once additional cloud opacity is exhausted. The net LW CRE profile being the difference between the downward and upward CRE profiles, i.e., something akin to a CRE “divergence”, mirrors more closely the downward CRE profile or the upward CRE profile (in absolute value) towards the boundary of the atmospheric column where each component is dominant, while it peaks where the two CRE profiles diverge the most.

Note that the upward and downward LW CRE profiles exhibit a progressive decrease of the height level where CRE saturates (upward) or reaches its peak (downward) as the CR index increases. This is a consequence of the general downward shift of cloudiness in our CR ordering. There are a few CR pairs that cannot be distinguished easily on the basis of their LW CRE profiles alone: CR4 and CR5; CR7 and CR8; CR10 and CR11. So while there are plenty of characteristics that make the members of these CR pairs distinct, the LW CRE profile is not one of them.

The SW CRE profiles (Fig. 11) are somewhat more straightforward to interpret, but also less intriguing. Upward and downward CRE profiles have similar shapes that follow each other closely with the exception of the atmospheric layers close to the surface where the downward CRE reduces (in absolute terms) slightly but abruptly probably because of water vapor reducing the contrast between downward clear-sky and all-sky fluxes. The change in slope for both profiles occurs where there is enough cloud of substantial optical thickness, and can be understood more easily by focusing on the downward CRE: the TOA value of zero remains intact until the topmost cloud layers are encountered by the

downward solar beam at which point the transmitted solar radiation for cloud-covered skies is drastically reduced. This interpretation helps us understand the progression of CRE profile “bending” points as one moves from high-cloud-rich to low-cloud-rich CRs. The reason a bending point is harder to identify for CR1 is because its upper level clouds are optically thinner and the reduction in downward solar radiation less dramatic. Because of the near-constant difference between the downward and upward CRE, the net CRE profiles are quite shapeless and hard to associate with cloud presence. An additional reason for the apparent featureless appearance of the net profiles is the use of the same scale as for the up and down CRE profiles. Yet, the variation with height of the net CRE profile is what determines CRH per eq. (4), and further explained below.

The LW and SW CRH profiles for each CR are shown in Fig. 12. Once again, the physical meaning of these profiles is that they show how much additional heating or cooling clouds provide to the atmosphere. As eq. (4) indicates, CRH is proportional to the derivative of the net CRE profiles, i.e. to the slope profile of the black curves of Figs. 10 and 11. As pointed out earlier, clouds provide additional heating of the atmosphere in the SW overall. Cooling contributions (negative values of CRH), however, are also seen, and they occur below the bulk of cloud occurrence characteristic of each regime. The levels at which cooling starts to occur (when descending from high to low altitudes) therefore shift as one progressively moves from high-cloud regimes (low CR indices) to low-cloud regimes (high CR indices). The cooling is of course explained by the reduction of solar radiation available to be absorbed by the water vapor underneath the bulk of cloudiness. The peak of positive CRH (heating) happens at the altitudes of local maximum in CF and

τ as long as a large fraction of the downward solar beam has survived its encounter with the clouds above.

The LW CRH curves of Fig. 12 also provide insight on how cloud-induced heating or cooling of the total atmospheric column inferred from Fig. 8 is achieved. The regimes below the diagonal in Fig. 8, CR1-5, characterized previously as warming regimes, realize the warming below the levels where most of the clouds occur and exhibit cooling above. The cooling regimes, CR6-11 exhibit cooling throughout most of the atmospheric column with peaks occurring near the top of where most of the cloudiness resides. The results shown here are not directly comparable to those of *Haynes et al.* [2013] who show latitude-height distributions of CRH, but are largely consistent if one considers the preferred areas of occurrence of our regimes.

The comparison between 2B-FLXHR-LIDAR LW CRE at TOA and CERES is left for the next subsection where AIRS TOA LW CRE is added as another comparison point. Here (Fig. 13) we show in step plot form only the comparison between LW and normalized SW CREs at the SFC (the SW TOA result does not provide much additional insight). The 2B-FLXHR-LIDAR variable used is BOACRE. Normalization is achieved simply by taking the ratio of standard CRE to incoming insolation at TOA. The CERES values come from the SYN1deg-3hr dataset with the 3-hour data point containing the selected 1:30 pm CC observation. The rationale for normalizing the SW CRE is to remove first order differences in the amount of incoming solar energy caused by the imperfect temporal matching.

The top panel of Fig. 13 summarizing the LW SFC CRE comparison reveals notable discrepancies between the two datasets for certain CRs. 2B-FLXHR-LIDAR

values tend to be larger for the CRs dominated by high cloud, the exception being the tropical CR1 where the values of SFC CRE are low because of its strong decoupling from cloud presence given the very humid environment. As we will see later, the discrepancy remains in the same direction also at TOA for these CRs. However, the difference between the two CREs reverses signs as more low clouds appear in higher index CRs. It is interesting to compare CRE contrasts among certain CRs internally within the two datasets. For instance the contrast between CR2 and CR1-CR3 is quite larger for CloudSat/CALIPSO than for CERES; but the former dataset exhibits much less contrast than the latter when CR6 is compared to CR5-CR7. Because SFC flux estimates involve radiative transfer calculation for both datasets, the specifics of cloud input (which come from different measurements) matter greatly for the eventual CRE values. CRs with low cloud fraction and simpler cloud structures, and therefore fewer ambiguities in the interpretation of the cloudy scene between active and passive measurements, have smaller disagreements in SFC LW CRE. One should also keep in mind that passive measurements have in general lower skill in locating cloud base altitude, a major driver of SFC LW CRE.

Turning our attention now to the comparison of normalized (as described above) SW SFC CRE, we note quite substantial inconsistencies for several regimes (CR1 to CR4; CR7 and CR9). The inconsistencies should not be surprising given the interpretation of (imperfectly matched in space and time) cloudiness by different observation systems, as explained above. Moreover, while the normalization accounts for the different amounts of incoming solar energy, it does not correct for the dependence of cloud reflectance and (more relevant for this case) transmittance on solar zenith angle.

619 Nevertheless, besides the aforementioned CRs, the agreement in normalized SW SFC
620 CRE is remarkable, and may be even fortuitous to some extent. The ordering of CR
621 strength with respect to this particular CRE measure is almost the same between the two
622 datasets; the sole exception is the opposite direction seen when going from CR8 to CR9.
623 In general, CRs are less distinct radiatively for CC. As characteristic examples, consider
624 the much smaller contrasts for CC between CR7 and CR8 (and also CR5-CR6) and
625 between CR9 and CR10 (the contrast between CR9 and CR8 being larger than CERES is
626 the notable exception).

627

628 *c) From AIRS*

629 The different radiative behavior of the various CRs in the thermal infrared spectral region
630 can also be gleaned by instantaneous values of LW TOA CRE inferred from the AIRS
631 OLR product discussed in subsection 2e. Fig. 14 compares then three LW TOA CRE
632 datasets, all for Aqua CR occurrences: CERES-SYN1deg-3hr (from the data points
633 containing the 1:30 pm observations of CC and AIRS), 2B-FLXHR-LIDAR, and AIRS.
634 Now we show the comparison in the form of a scatterplot with the CERES values on the
635 x-axis used as “reference” for the purposes of the discussion. CERES and AIRS cover the
636 same 12-year period, while 2B-FLXHR-LIDAR a much shorter period of four years. A
637 systematic pattern can be immediately seen: blue points (AIRS) tend to appear below the
638 black diagonal, indicating values lower than those from CERES, while the opposite is
639 seen for 2B-FLXHR-LIDAR data. The differences tend of course to be smaller in
640 absolute value for the low-cloud dominated regimes for which the LW CRE is weaker.
641 For CR2, the regime with the strongest LW CRE at TOA, the AIRS-CC discrepancy is

quite large, about $\sim 25 \text{ Wm}^{-2}$ with AIRS differing slightly more from CERES than CC despite interannual variations not being a factor.

Part of the discrepancies between CERES and the other two datasets can be attributed to the fact that the CERES values are not strictly speaking 1:30 pm values, but three-hour averages around that point in time. But this does obviously not explain why AIRS and 2B-FLXHR-LIDAR tend to be on opposite sides of the diagonal since the observations are almost exactly contemporaneous (although imperfectly collocated spatially – something that would produce random differences). Since for both these datasets CRE comes from radiative transfer calculations that use as input different interpretations of cloudiness within their field of view, one from passive infrared measurements, the other from active observations, it may not come as a surprise that the biggest discrepancies occur for the regimes, like CR2, with the most complex cloud structure.

The systematically lower values of AIRS prompted us to conduct additional investigation. Specifically, we looked at AIRS OLR availability as a function of MODIS gridcell A_c values for each CR. We found that the fraction of available AIRS OLR values given the existence of a MODIS CR decreased with A_c . This is apparently related to the progressively reduced ability to retrieve temperature and moisture profiles (needed for the radiation calculations that produce the OLR and hence CRE) as AIRS footprints become more cloudy [Tian *et al.* 2013]. When $A_c > 0.9$ in the $1^\circ \times 1^\circ$ gridcell, an AIRS OLR was available only 82% of the time. The availability fraction of AIRS OLR in this CF range is much less for certain CRs, notably CR1, CR2, and CR11 with availability fractions of 0.59, 0.65, and 0.63 respectively. Given the linear dependence of gridcell

CRE to A_c per eq. (1), it is not surprising that the many missing OLRs at the highest CFs make the AIRS LW CREs to be biased toward smaller values.

With CC- and AIRS-based LW TOA CREs being systematically, higher and lower than CERES, respectively, an obvious question is whether the ranking of CRs in terms of their contribution to the global CRE is affected. The answer can be sought in Fig. 15 which is a scatterplot similar to that of Fig. 14, but with percent contributions plotted this time. There is no doubt about the two CRs with the strongest contributions, shown separately in the inset. All datasets agree on the contribution values of CR12 which is driven forcefully by this regime's dominant RFO; but CR3 is more important for AIRS than for the other two datasets. For the third ranked CR there are interesting differences among the datasets: it is CR2 for 2B-FLXHR-LIDAR, far exceeding CR1, which tops CR2 for AIRS, but with less contribution contrast; for CERES, however, these two regimes contribute about the same. CR4-CR5 are little different for 2B-FLXHR-LIDAR and CERES, but more different, and with order reversed, for AIRS. Note that in contrast with Fig. 14, points for both datasets being compared to CERES have to lie on both sides of the diagonal in this plot since the sum of values for all three datasets must add to 100% by design.

5. Discussion and Conclusions

We have updated the MODIS cloud regimes of previous work using newer versions of retrieved cloud properties from the Collection 6 processing algorithm. With the new regimes in hand, we provide detailed insight of how cloud mesoscale organizations as expressed via these regimes affect the radiation budget of the planet. We have expanded

substantially previous investigations of this problem by using multiple sources of radiative flux information which helps us conduct the most complete to date analysis of cloud radiative effect breakdown based on the cloud regime concept. The availability of multiple datasets allows numerous illuminating comparisons. Any differences seen do not diminish the remarkable consistency among the datasets and the coherent picture between our interpretation of the makeup of the regimes and their radiative character. The radiative insight provided in this paper is greatly enhanced by our ability to construct vertical profiles of cloud effects on radiative fluxes and heating/cooling rates by capitalizing on the ability to spatiotemporally match to an adequate degree MODIS-Aqua and CloudSat/CALIPSO observations, all part of the A-Train constellation.

Decomposing the effects of clouds based on the cloud regime concept makes sense in many respects. Cloud regimes can be ranked based on their radiative importance and their mean instantaneous (at the time of occurrence) impact can be contrasted with their long-term impact which also depends on the frequency at which they occur. We were able to distinguish regimes based on whether they radiatively cool or warm the atmosphere, and thanks to radiative heating profiles identify the atmospheric levels at which the cooling and warming tends to materialize. Terra and Aqua comparisons allowed us to get some sense of whether differences in morning or afternoon occurrences of particular regimes make them matter more or less radiatively. Multiple irradiance datasets enabled us to examine the regimes for which radiative discrepancies between contemporaneous observations are pronounced or subdued. Furthermore, these datasets put us in a position to surmise whether the discrepancies were related to the complexity of cloud structure, its interpretation by different observational systems, and its subsequent

representation in forward radiative transfer calculations, or to the uneven sampling caused by retrieval limitations.

Other papers have discussed how CRs can be employed to evaluate the quality of Global Climate Model clouds, including papers that have targeted regime and CRE links under both present and future climates [Williams and Webb 2009; Tsushima et al. 2013]. The results of this investigation facilitate such studies since they provide additional observational constraints to test the models. Comparison of radiative regime-based flux composites can be used as complementary to geographical comparisons for better understanding of whether problematic radiation climatologies in models come from inherent problems in cloud and radiation simulations or from placing otherwise realistic cloud systems at incorrect locations.

Acknowledgements

Funding from NASA's Modeling Analysis and Prediction, CloudSat/CALIPSO, and the Science of Terra and Aqua programs is gratefully acknowledged. Please contact the lead author for obtaining the MODIS cloud regime data used in this paper. Data used for this paper come from the following sources: MODIS data were obtained from <https://ladsweb.nascom.nasa.gov>; CloudSat/CALIPSO data from <http://www.cloudsat.cira.colostate.edu>; CCCM data from https://eosweb.larc.nasa.gov/project/ceres/cccm_table; CERES data from https://eosweb.larc.nasa.gov/project/ceres/ceres_table; AIRS data from <http://disc.sci.gsfc.nasa.gov/uui/search/%22AIRS%22>; and MERRA data from <http://disc.sci.gsfc.nasa.gov/mdisc/>.

734

735 **References**

736 Anderberg, M. R., 1973: Cluster Analysis for Applications, 359 pp., Elsevier, New York.

737 Doelling D. R., N. G. Loeb, D. F. Keyes, M. L. Nordeen, D. Morstad, C. Nguyen, B. A.

738 Wielicki, D. F. Young, and M. Sun, (2013), Geostationary enhanced temporal

739 interpolation for CERES flux products, *J. Atmos. Oceanic Technol.*, 30, 1072–1090,

740 doi: <http://dx.doi.org/10.1175/JTECH-D-12-00136.1>

741 Harrison, E. F., P. Minnis, B. R. Barkstrom, V. Ramanathan, R. D. Cess, and G. G.

742 Gibson (1990), Seasonal variation of cloud radiative forcing derived from the Earth

743 Radiation Budget Experiment, *J. Geophys. Res.*, 95, 18,687–18,703,

744 doi:[10.1029/JD095iD11p18687](http://dx.doi.org/10.1029/JD095iD11p18687).

745 Haynes, J. M., T. H. Vonder Haar, T. L'Ecuyer, and D. Henderson (2013), Radiative

746 heating characteristics of Earth's cloudy atmosphere from vertically resolved active

747 sensors, *Geophys. Res. Lett.*, 40, 624–630, doi:[10.1002/grl.50145](http://dx.doi.org/10.1002/grl.50145).

748 Henderson, D. S., T. L'Ecuyer, G. L. Stephens, P. Partain, and M. Sekiguchi (2013), A

749 multisensor perspective on the radiative impacts of clouds and aerosols., *J. Appl.*

750 *Meteor. Climatol.*, 52, 853-871.

751 Iacono, M. J., J. S. Delamere, E. J. Mlawer, M. W. Shephard, S. A. Clough, and W. D.

752 Collins (2008), Radiative forcing by long-lived greenhouse gases: Calculations with

753 the AER radiative transfer models, *J. Geophys. Res.*, 113, D13103,

754 doi:[10.1029/2008JD009944](http://dx.doi.org/10.1029/2008JD009944).

755 Jakob, C., and G. Tselioudis (2003), Objective identification of cloud regimes in the

756 tropical western Pacific, *Geophys. Res. Lett.*, 30, doi:10.1029/2003GL018367.

757 Kato, S., S. Sun-Mack, W. F. Miller, F. G. Rose, Y. Chen, P. Minnis, and B. A. Wielicki
 758 (2010), Relationships among cloud occurrence frequency, overlap, and effective
 759 thickness derived from CALIPSO and CloudSat merged cloud vertical profiles, *J.*
 760 *Geophys. Res.*, *115*, D00H28, doi:10.1029/2009JD012277.

761 Kato, S., F. G. Rose, S. Sun-Mack, W. F. Miller, Y. Chen, D. A. Rutan, G. L. Stephens,
 762 N. G. Loeb, P. Minnis, B. A. Wielicki, D. M. Winker, T. P. Charlock, P. W.
 763 Stackhouse, K.-M. Xu, and W. J. Collins (2011), Improvements of top-of-atmosphere
 764 and surface irradiance computations with CALIPSO, CloudSat, and MODIS derived
 765 cloud and aerosol properties, *J. Geophys. Res.*, *116*, D19209,
 766 doi:10.1029/2011JD16050.

767 King, M. D., S. Platnick, P. A. Hubanks, G. T. Arnold, E. G. Moody, G. Wind, and B.
 768 Wind, (2006), Collection 005 change summary for the MODIS cloud optical property
 769 (06_OD) algorithm. NASA Rep., Version 3.1, 23 pp. [Available online at
 770 [http://modis-](http://modis-atmos.gsfc.nasa.gov/C005_Changes/C005_CloudOpticalProperties_ver311.pdf)
 771 [atmos.gsfc.nasa.gov/C005_Changes/C005_CloudOpticalProperties_ver311.pdf](http://modis-atmos.gsfc.nasa.gov/C005_Changes/C005_CloudOpticalProperties_ver311.pdf).]

772 L'Ecuyer, T. S., N. B. Wood, T. Haladay, G. L. Stephens, and P. W. Stackhouse Jr.
 773 (2008), Impact of clouds on atmospheric heating based on the R04 CloudSat fluxes
 774 and heating rates data set, *J. Geophys. Res.*, *113*, D00A15,
 775 doi:[10.1029/2008JD009951](https://doi.org/10.1029/2008JD009951).

776 L'Ecuyer, T. S., and J. H. Jiang (2010), Touring the atmosphere aboard the A-Train,
 777 *Phys. Today*, 63(7), 36–41, doi:[10.1063/1.3463626](https://doi.org/10.1063/1.3463626).

778 Lee, D., L. Oreopoulos, G. J. Huffman, W. B. Rossow, and I.-S. Kang (2013), The
 779 precipitation characteristics of ISCCP tropical weather states, *J. Climate*, 26, 772-
 780 788, doi: <http://dx.doi.org/10.1175/JCLI-D-11-00718.1>.
 781 Mason S., C. Jakob, A. Protat, and J. Delanoë, (2014), Characterizing observed
 782 midtopped cloud regimes associated with southern ocean shortwave radiation biases.
 783 *J. Climate*, 27, 6189–6203, doi: <http://dx.doi.org/10.1175/JCLI-D-14-00139.1>
 784 Oreopoulos, L., and W. Rossow (2011), The cloud radiative effects of International
 785 Satellite Cloud Climatology Project weather states, *J. Geophys. Res.*, 116,
 786 doi:10.1029/2010JD015472.
 787 Oreopoulos, L., N. Cho, D. Lee, S. Kato, and G. J. Huffman (2014), An examination of
 788 the nature of global MODIS cloud regimes, *J. Geophys. Res. Atmos.*, 119, 8362–
 789 8383, doi:[10.1002/2013JD021409](http://dx.doi.org/10.1002/2013JD021409).
 790 Pagano, T. S., H. H. Aumann, D. E. Hagan, and K. Overoye (2003), Prelaunch and in-
 791 flight radiometric calibration of the Atmospheric Infrared Sounder (AIRS), *IEEE*
 792 *Trans. Geosci. Remote Sens.*, 41, 265–273, doi:[10.1109/TGRS.2002.808324](http://dx.doi.org/10.1109/TGRS.2002.808324).
 793 Pincus, R., S. Platnick, S. Ackerman, R. Hemler, and R. Hofmann (2012), Reconciling
 794 simulated and observed views of clouds: MODIS, ISCCP, and the limits of
 795 instrument simulators, *J. Clim.*, 25, 4699–4720, doi:10.1175/JCLI-D-11-00267.1.
 796 Rienecker, M., et al. (2011), MERRA: NASA's Modern-Era Retrospective Analysis for
 797 research and applications, *J. Clim.*, 24, 3624–3648, doi:10.1175/JCLI-D-11-00015.1.
 798 Rossow, W., G. Tselioudis, A. Polak, and C. Jakob (2005), Tropical climate described as
 799 a distribution of weather states indicated by distinct mesoscale cloud property
 800 mixtures, *Geophys. Res. Lett.*, 32, doi:10.1029/2005GL024584.

Rutan D. A., S. Kato, D. R. Doelling, F. G. Rose, L. T. Nguyen, T. E. Caldwell, and N. G. Loeb, (2015), CERES synoptic product: methodology and validation of surface radiant flux. *J. Atmos. Oceanic Technol.*, 32, 1121–1143, doi: <http://dx.doi.org/10.1175/JTECH-D-14-00165.1>

Stephens, G. L., et al. (2012), An update on Earth's energy balance in light of the latest global observations, *Nat. Geosci.*, 5, 691–696, doi: [10.1038/ngeo1580](https://doi.org/10.1038/ngeo1580).

Susskind, J., G. Molnar, L. Iredell, and N. G. Loeb (2012), Interannual variability of outgoing longwave radiation as observed by AIRS and CERES, *J. Geophys. Res.*, 117, D23107, doi: [10.1029/2012JD017997](https://doi.org/10.1029/2012JD017997).

Tan, J., C. Jakob, W.B. Rossow, and G. Tselioudis, 2015: [Increases in tropical rainfall driven by changes in frequency of organized deep convection](https://doi.org/10.1038/nature14339). *Nature*, **519**, 451-454, doi:10.1038/nature14339.

Tian, B., E. Fetzer, B. Kahn, J. Teixeira, E. Manning, and T. Hearty (2013), Evaluating CMIP5 models using AIRS tropospheric air temperature and specific humidity climatology, *J. Geophys. Res.*, 118, 114-134, doi:10.1029/2012JD018607.

Tselioudis, G., E. Tromeur, W. B. Rossow, and C. S. Zerefos (2010), Decadal changes in tropical convection suggest effects on stratospheric water vapor, *Geophys. Res. Lett.*, 37, L14806, doi: [10.1029/2010GL044092](https://doi.org/10.1029/2010GL044092).

Tselioudis, G., W. B. Rossow, Y. Zhang, and D. Konsta (2013), Global weather states and their properties from passive and active satellite cloud retrievals. *J. Climate*, 26, 7734–7746, doi: <http://dx.doi.org/10.1175/JCLI-D-13-00024.1>

822 Tsushima Y., M. A. Ringer, M. J. Webb, and K. D. Williams (2013), Quantitative
823 evaluation of the seasonal variations in climate model cloud regimes, *Clim. Dyn.* 41,
824 2679–2696. doi: 10.1007/s00382-012-1609-4.

825 Williams K. D., and M. J. Webb (2009), A quantitative performance assessment of cloud
826 regimes in climate models, *Clim. Dyn.*, 33, 141–157, doi:10.1007/s00382-008-0443-1.

827 Zhang, Y., W. B. Rossow, A. A. Lacis, V. Oinas, and M. I. Mishchenko (2004),
828 Calculation of radiative fluxes from the surface to top of atmosphere based on ISCCP
829 and other global data sets: Refinements of the radiative transfer model and the input
830 data, *J. Geophys. Res.*, 109, D19105, doi:[10.1029/2003JD004457](https://doi.org/10.1029/2003JD004457).

831 Zhang, Z., and S. Platnick (2011), An assessment of differences between cloud effective
832 particle radius retrievals for marine water clouds from three MODIS spectral bands, *J.*
833 *Geophys. Res.*, 116, D20215, doi:[10.1029/2011JD016216](https://doi.org/10.1029/2011JD016216).

834

List of Figures

Figure 1. Centroids (mean histograms) of the twelve Cloud Regimes (CRs) derived from clustering analysis on 12-years of MODIS C6 Aqua-Terra p_c - τ joint daily histograms at a resolution of 1° . Additional information included in each panel is the mean global cloud fraction CF and Relative Frequency of Occurrence (RFO) of each CR.

Figure 2. The geographical multi-annual mean RFO of each of the twelve MODIS C6 CRs.

Figure 3. Boxplot of the 500 hPa large-scale vertical velocity associated with each CR, derived from compositing MERRA data. The box length indicates the interquartile range, the horizontal line is the median, and the symbol represents the mean.

Figure 4. Liquid, ice, and total CF for each CR derived from compositing gridded MODIS A_c values. The total A_c values are slightly above the sum of liquid and ice A_c because of pixels of undetermined thermodynamic phase.

Figure 5. Percent fraction of cloud types within each occurrence of a MODIS Aqua CR for which CloudSat cloud type information from the 2B-CLDCLASS product (as aggregated in the C3M dataset) was also available. The last bar “C3M” shows cloud type fractions for the entire Aqua CR dataset for which there is spatiotemporal overlap.

Standard two-letter abbreviations have been used for the various cloud types, namely:

Cb =cumulonimbus; Ci =cirrus; As =altostratus; Ac =altocumulus, Ns =nimbostratus;

St =stratus; Sc =stratocumulus; Cu =cumulus.

Figure 6. CERES SYN1deg daily LW and SW TOA CRE for the period Dec. 1, 2002 to Nov. 30, 2014 composited (by taking latitudinally-weighted averages) by MODIS CR.

Only gridcells with the same Terra and Aqua CR are considered. The horizontal and vertical error bars indicate one fifth of the interquartile range of the distributions used to calculate the composite means; distance from median to 25% percentile is represented by the error bars below and to the left of the symbol while that to the 75% percentile by the error bars above and to the right. The diagonal lines are isolines of constant $total=SW+LW$ CRE at 20 Wm^{-2} increments. Net (=down-up) fluxes were used for the calculation of CRE per eq. (1).

Figure 7. Counterpart to Fig. 6, but for SW, LW and *total* percent CRE contributions obtained by dividing each CR's sum of CREs by the sum of all available CRE values (for gridcells obeying the restriction of Fig. 6). These contributions therefore account for the CR RFOs. A separate scale is used for CR12, the largest contributor (inset). The diagonal lines are isolines of constant *total* CRE contribution at 5% increments.

Figure 8. CERES SYN1deg daily LW SFC against LW TOA CRE composited by MODIS CR for the gridcells obeying the restriction of Fig. 6. Horizontal and vertical error bars are drawn with the same conventions as Fig. 6, but now represent half the interquartile range.

Figure 9. “Step” plot comparing LW and SW TOA CRE between Terra and Aqua. The top two panels show mean CRE composites (meaning is the same as in Fig. 6). The bottom two panels show percent contributions (meaning is the same as in Fig. 7, but relative to the individual Terra and Aqua CRE global sums).

Figure 10. LW CRE profile composites by CR from the 2B-FLXHR-LIDAR dataset. Each panel shows three profiles for upward, downward and net (=downward-upward) CRE. The value of the TOA net CRE is shown also at the lower abscissa to facilitate

comparison with the SFC value, so that the warming (when greater than the SFC value) or cooling (when smaller than the SFC value) can be easily inferred. Note that the x-axis scale is different for CR2 and CR3.

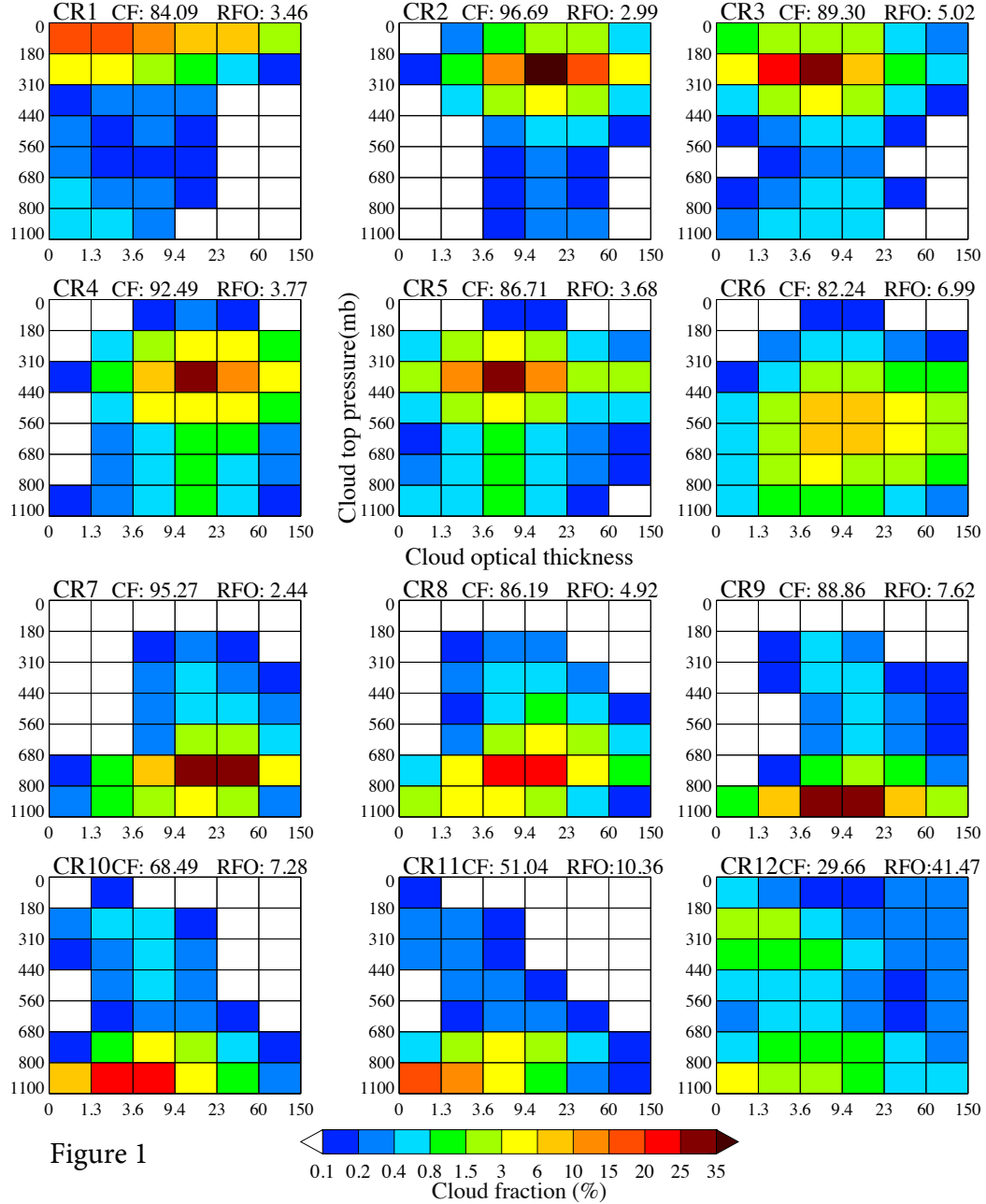
Figure 11. As in Fig. 10, but for SW CRE. Note that the x-axis scale is different for CR2.

Figure 12. Composite profiles by CR of LW and SW CRH defined by eq. (4).

Figure 13. Comparison of CERES-SYN1deg-3hr composite SFC CRE by CR with that from CC (2B-FLXHR-LIDAR) for Aqua CR occurrences, in the form of a “step” plot. The data period is different as explained in the text. The upper panel shows a comparison of LW SFC CRE while the lower panel a comparison between normalized SW SFC CRE.

Figure 14. Scatterplot comparing composite (mean) LW CRE values at TOA by CR among CERES SYN1deg-3hr, 2B-FLXHR-LIDAR and AIRS for Aqua CR occurrences. The period of 2B-FLXHR-LIDAR data is different from that of the other two as explained in the text. Besides the black dashed diagonal of equal values, we also plot least-square fit lines for 2B-FLXHR-LIDAR (red line) and AIRS (blue line) data. The region of the plot within the square has been enhanced and is shown as an inset.

Figure 15. Scatterplot comparing the contribution to the global LW TOA CRE by CR among CERES SYN1deg-3hr, 2B-FLXHR-LIDAR and AIRS for Aqua CR occurrences. The period of 2B-FLXHR-LIDAR data is different from that of the other two as explained in the text. The comparison for the two CRs that are the biggest contributors is shown separately as an inset.



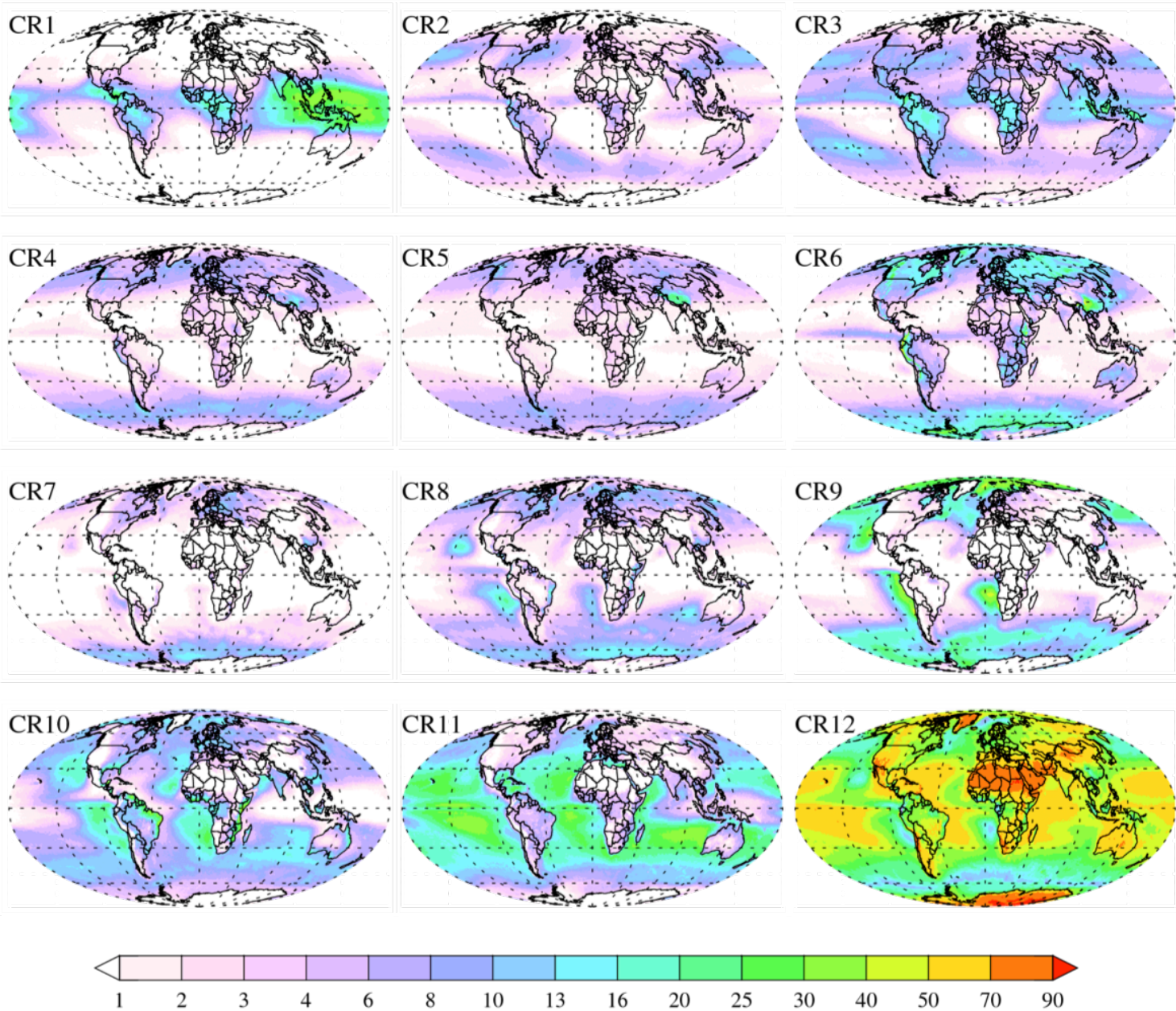
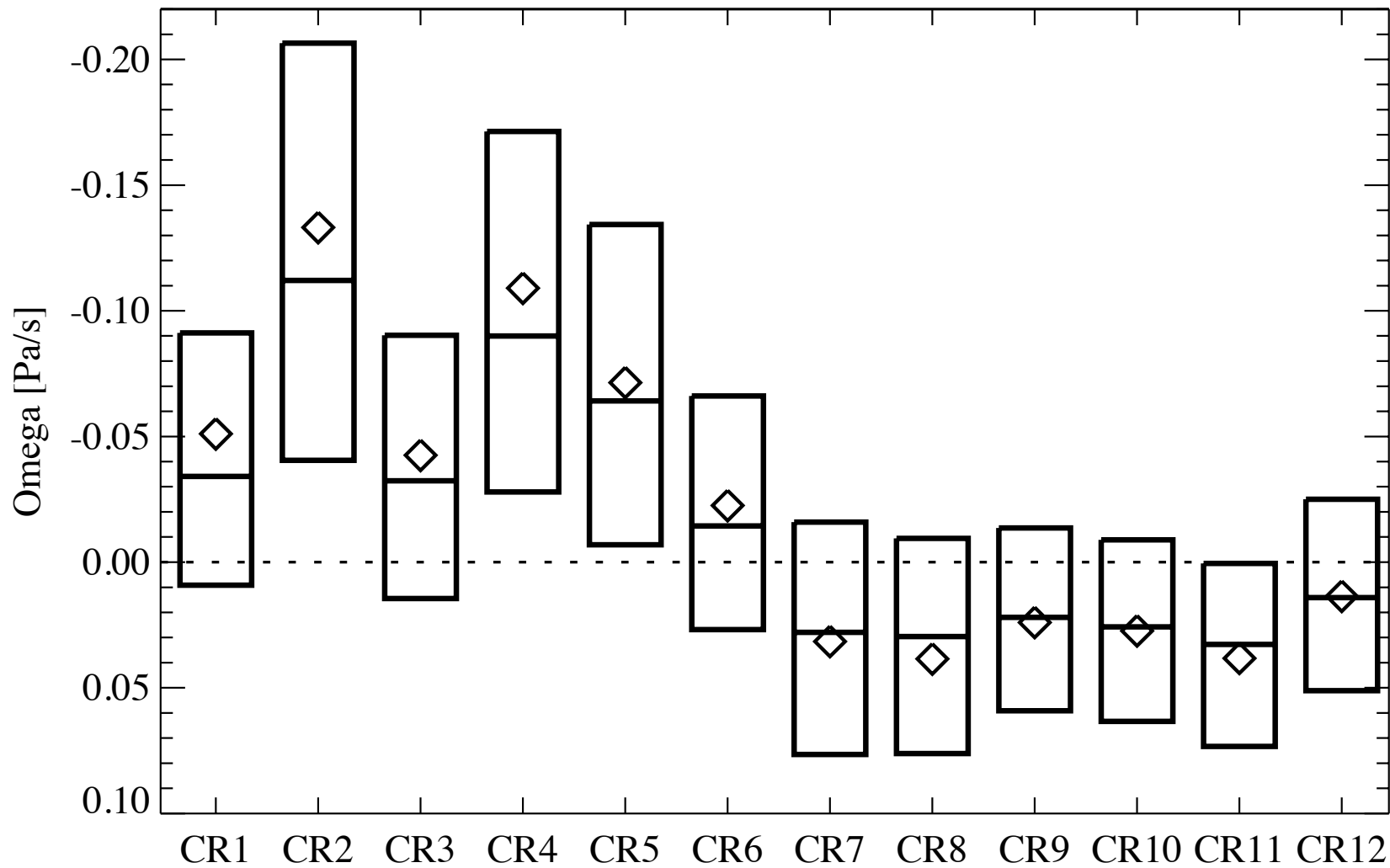


Figure 2

RFO (%)

Figure 3



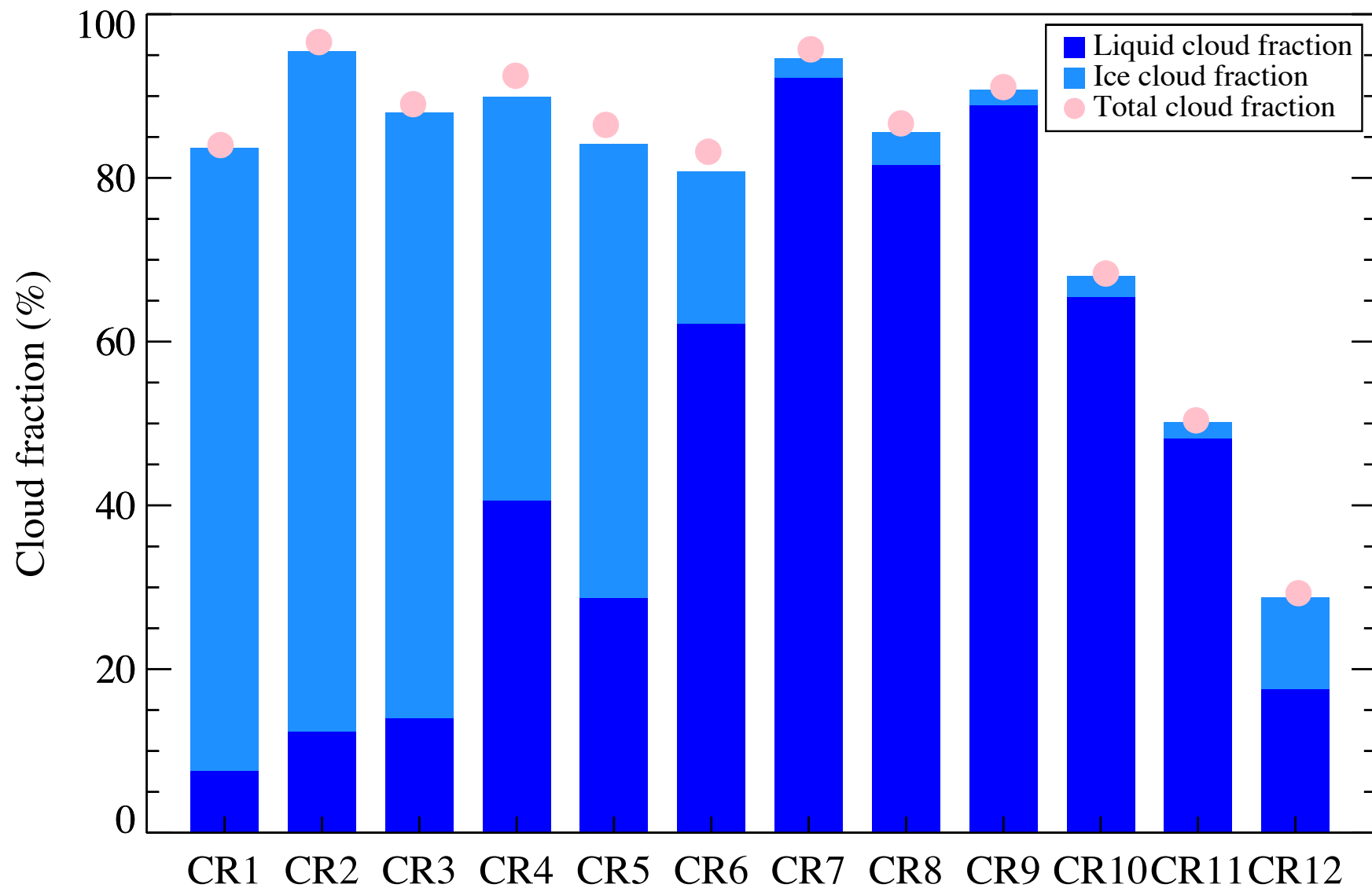


Figure 4

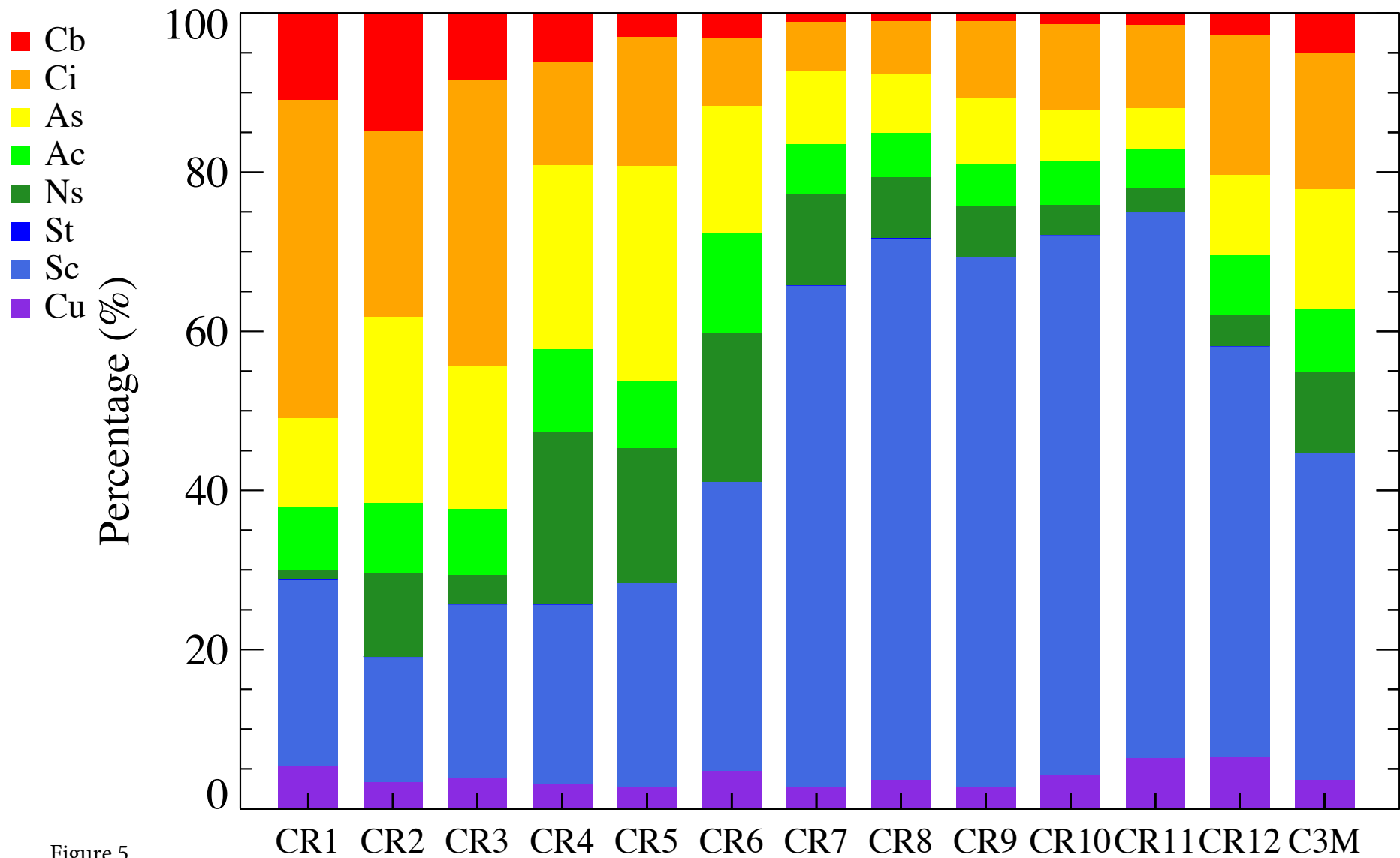


Figure 5

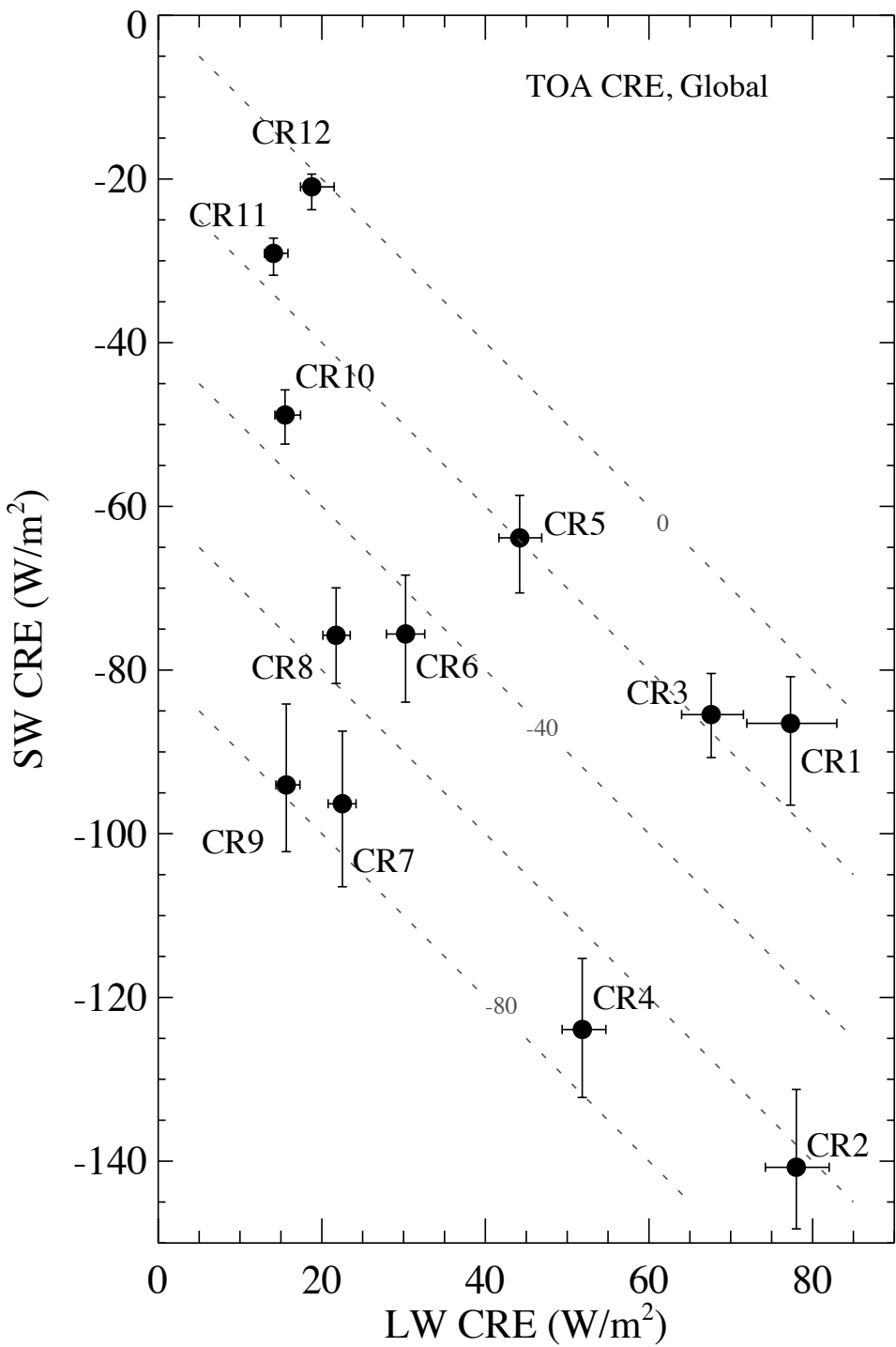
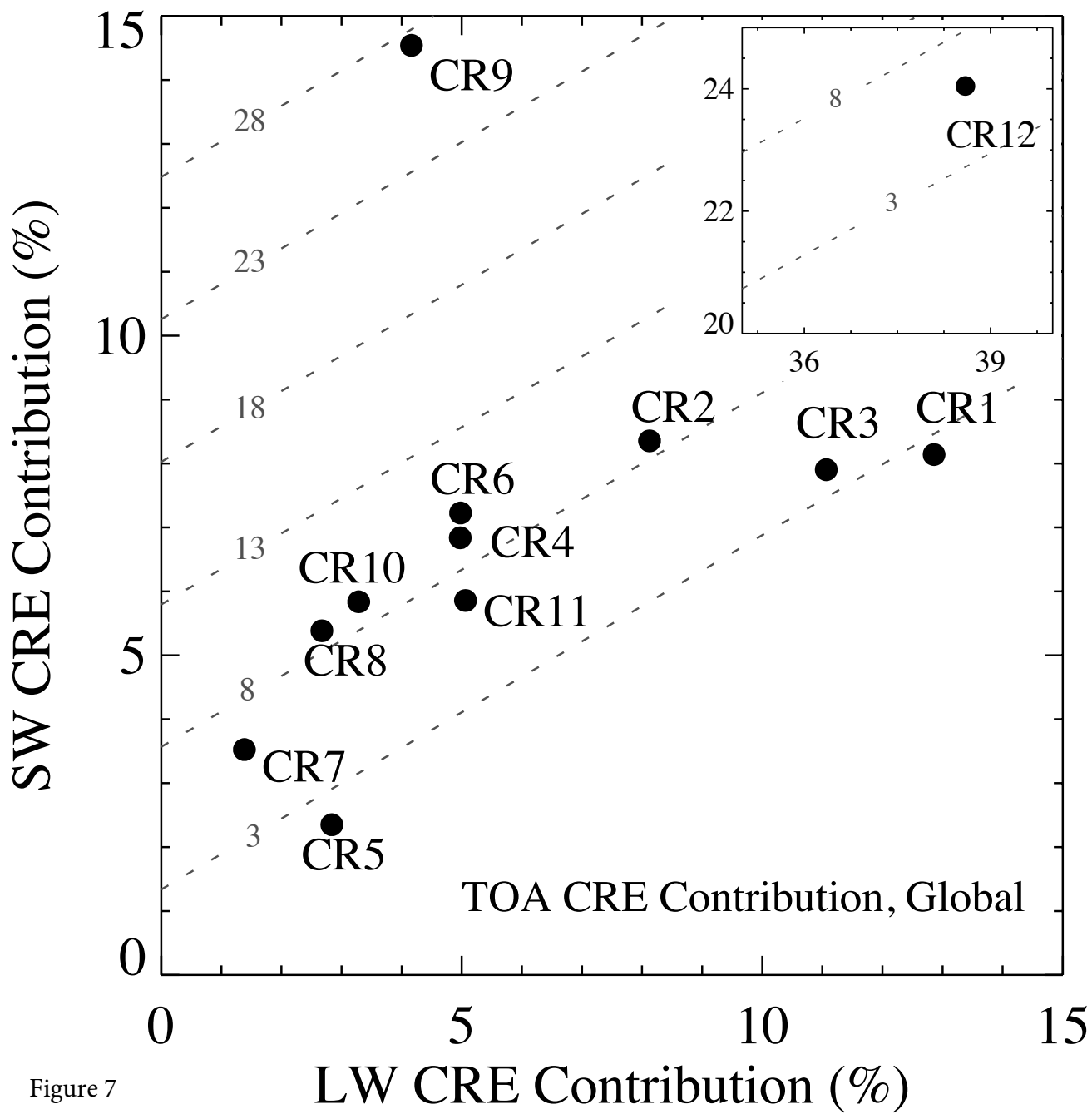


Figure 6



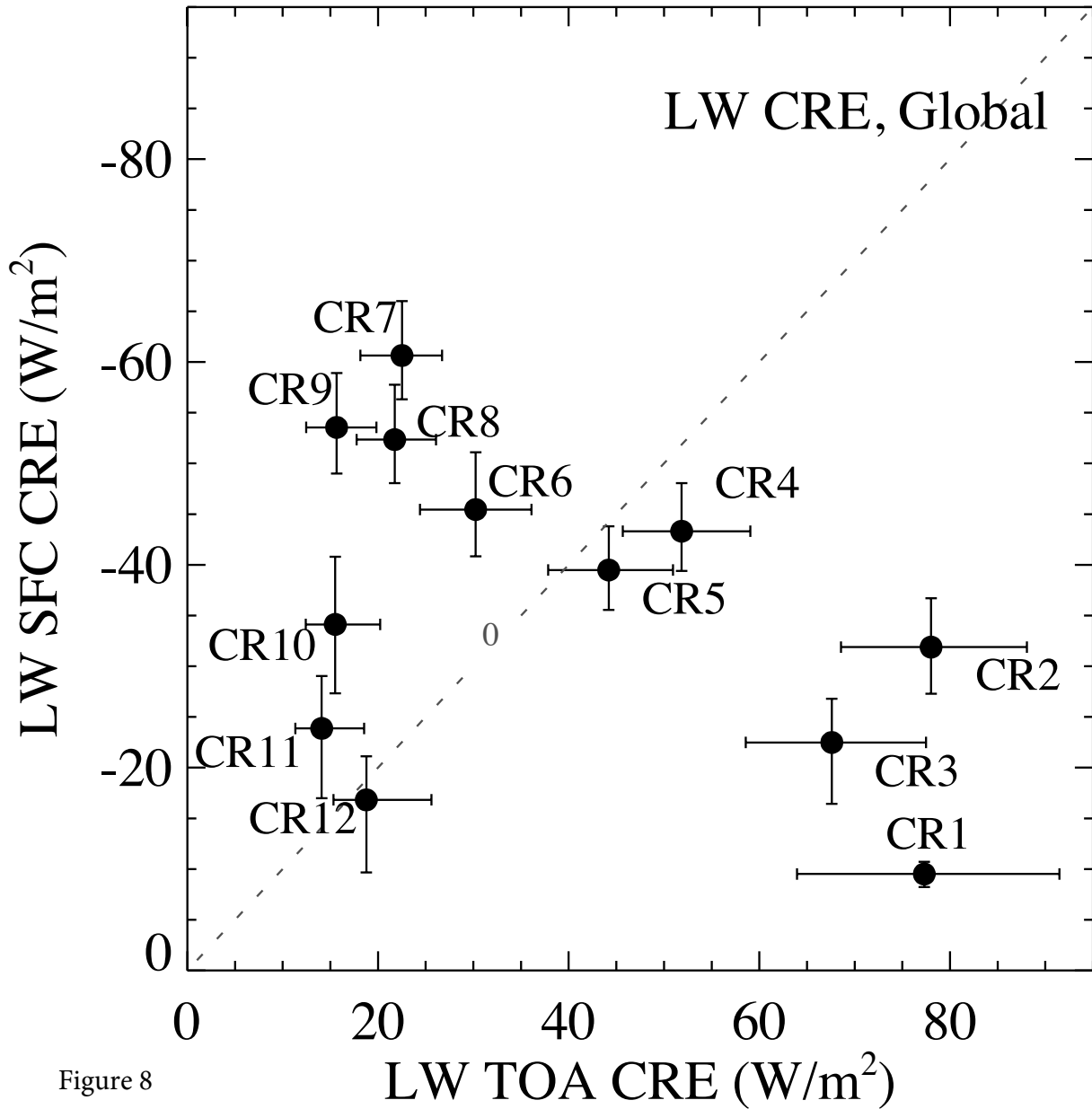


Figure 8

Figure 9

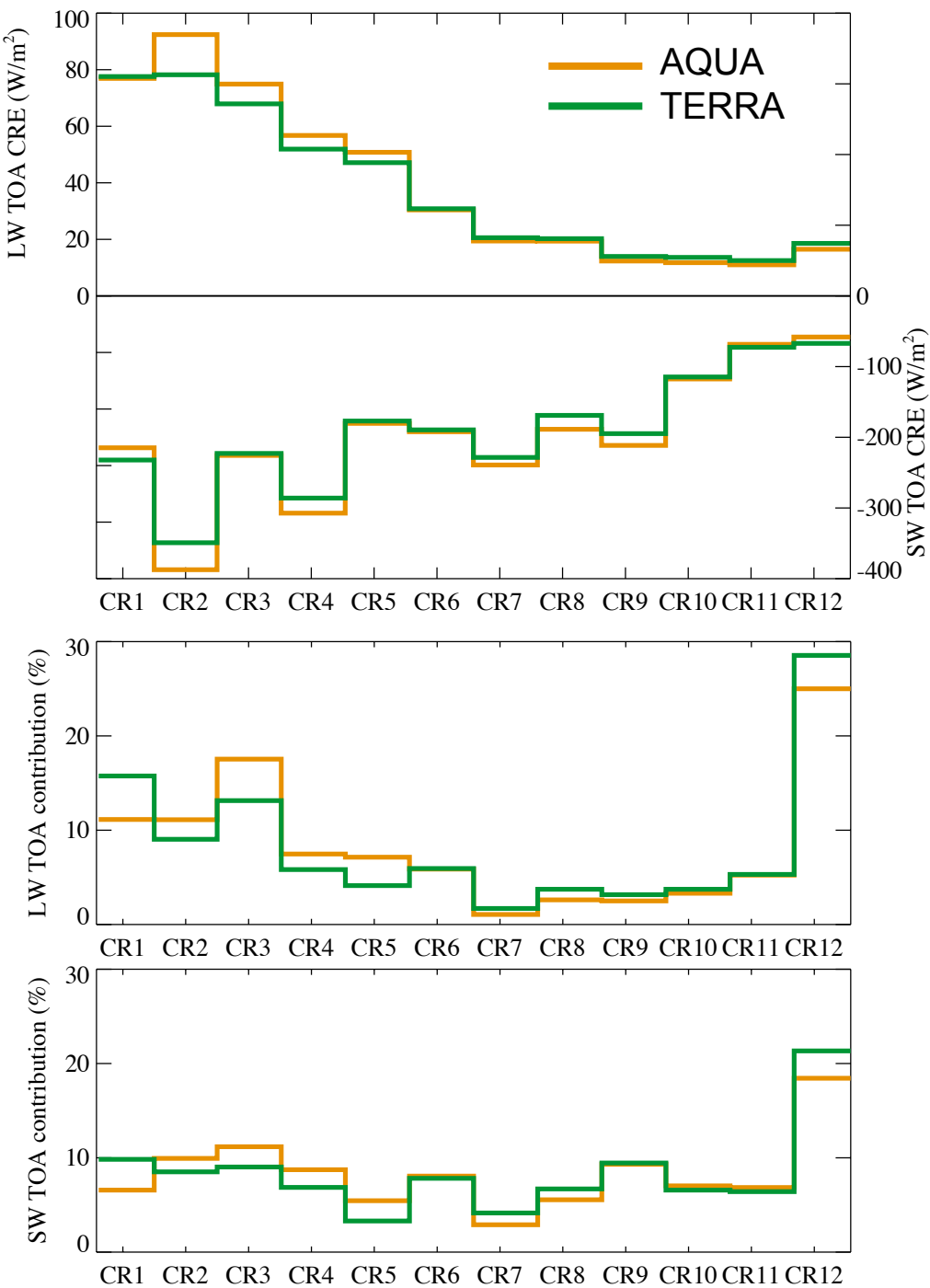


Figure 10

— Upward LW CRE
— Downward LW CRE
— NET LW CRE : $[F_{\downarrow} - F_{\uparrow}]_{\text{all}} - [F_{\downarrow} - F_{\uparrow}]_{\text{clr}}$

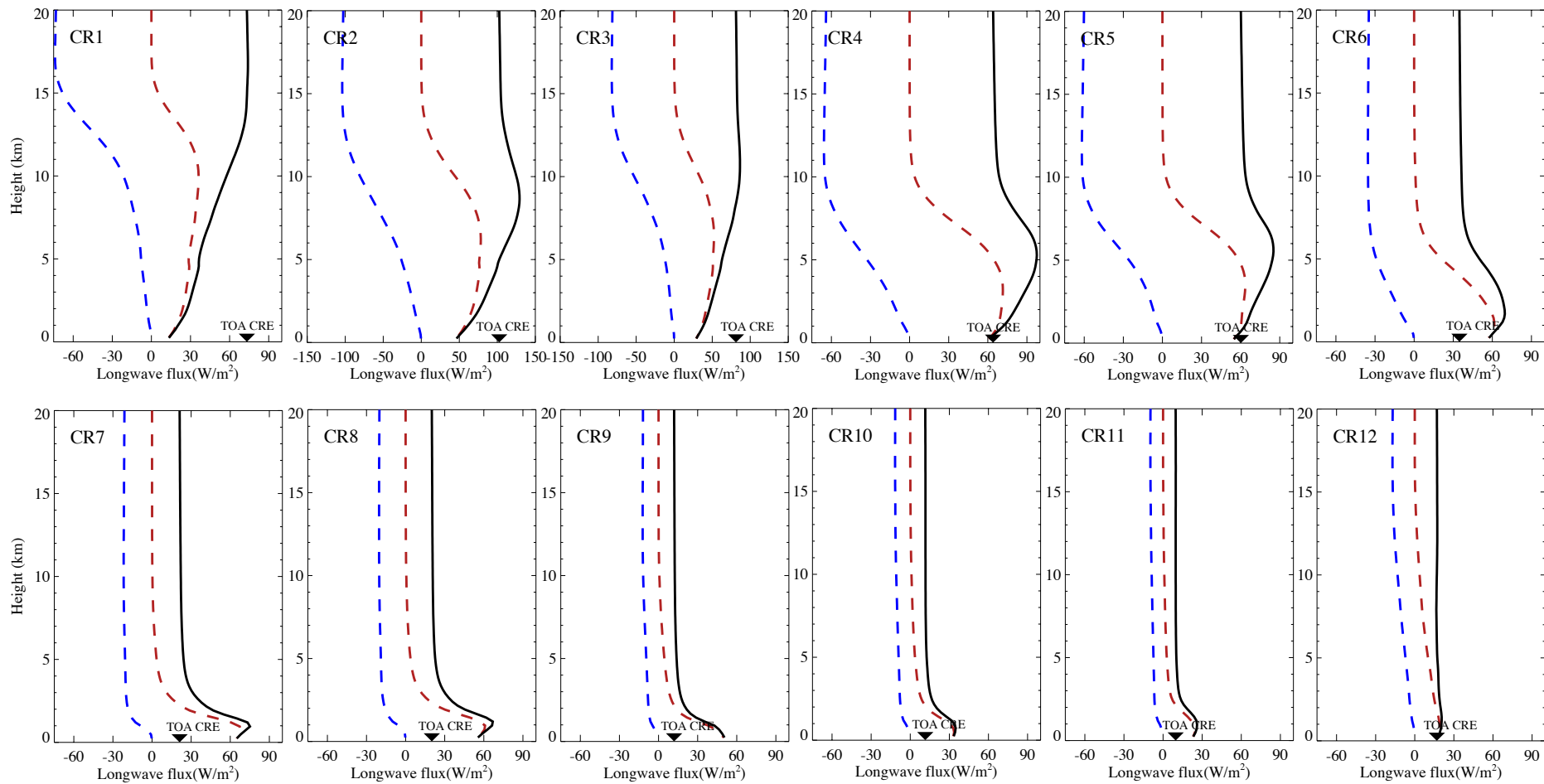
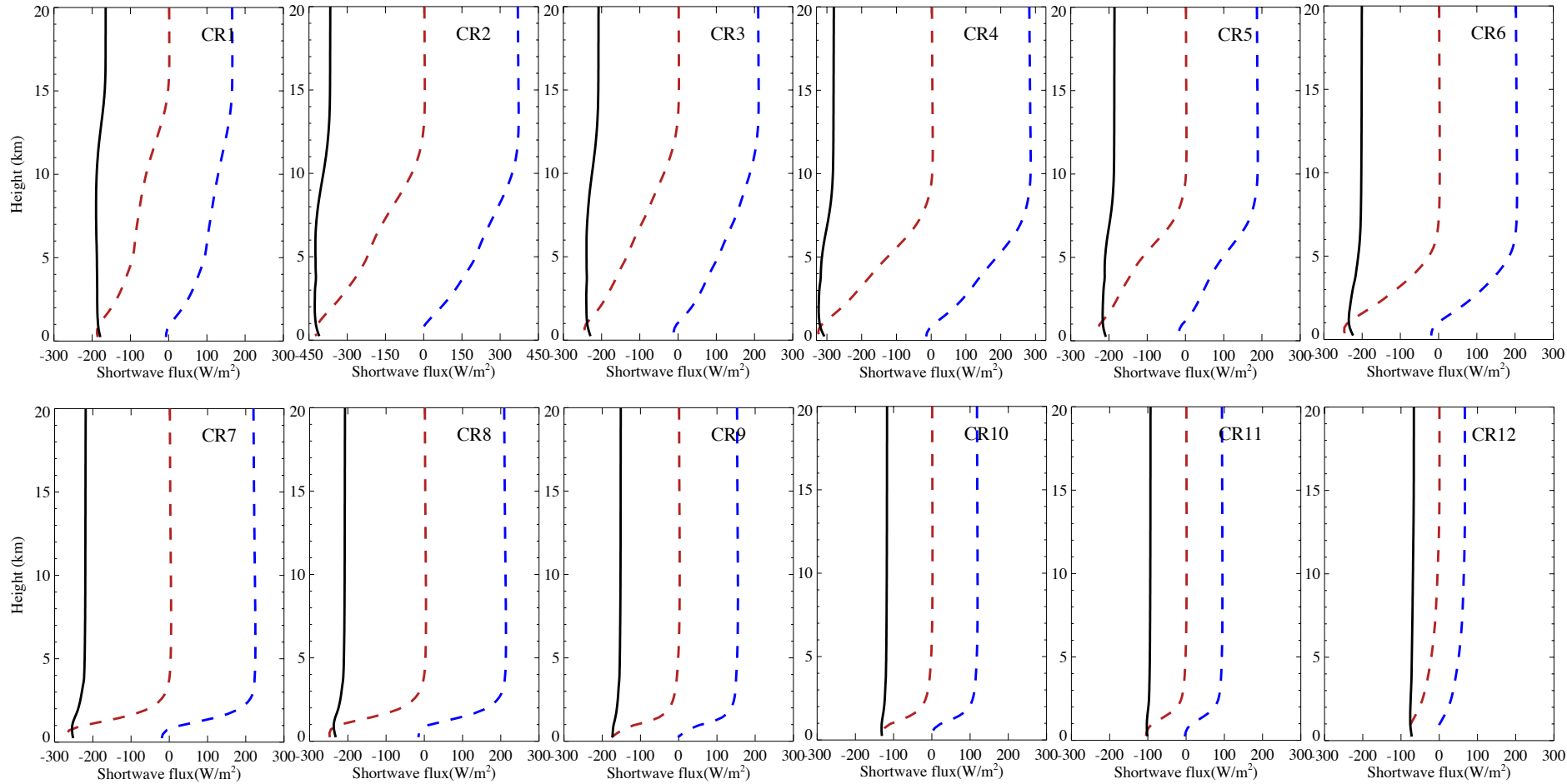


Figure 11

— Upward SW CRE
--- Downward SW CRE
— NET SW CRE : $[F_{\downarrow} - F_{\uparrow}]_{\text{all}} - [F_{\downarrow} - F_{\uparrow}]_{\text{clr}}$



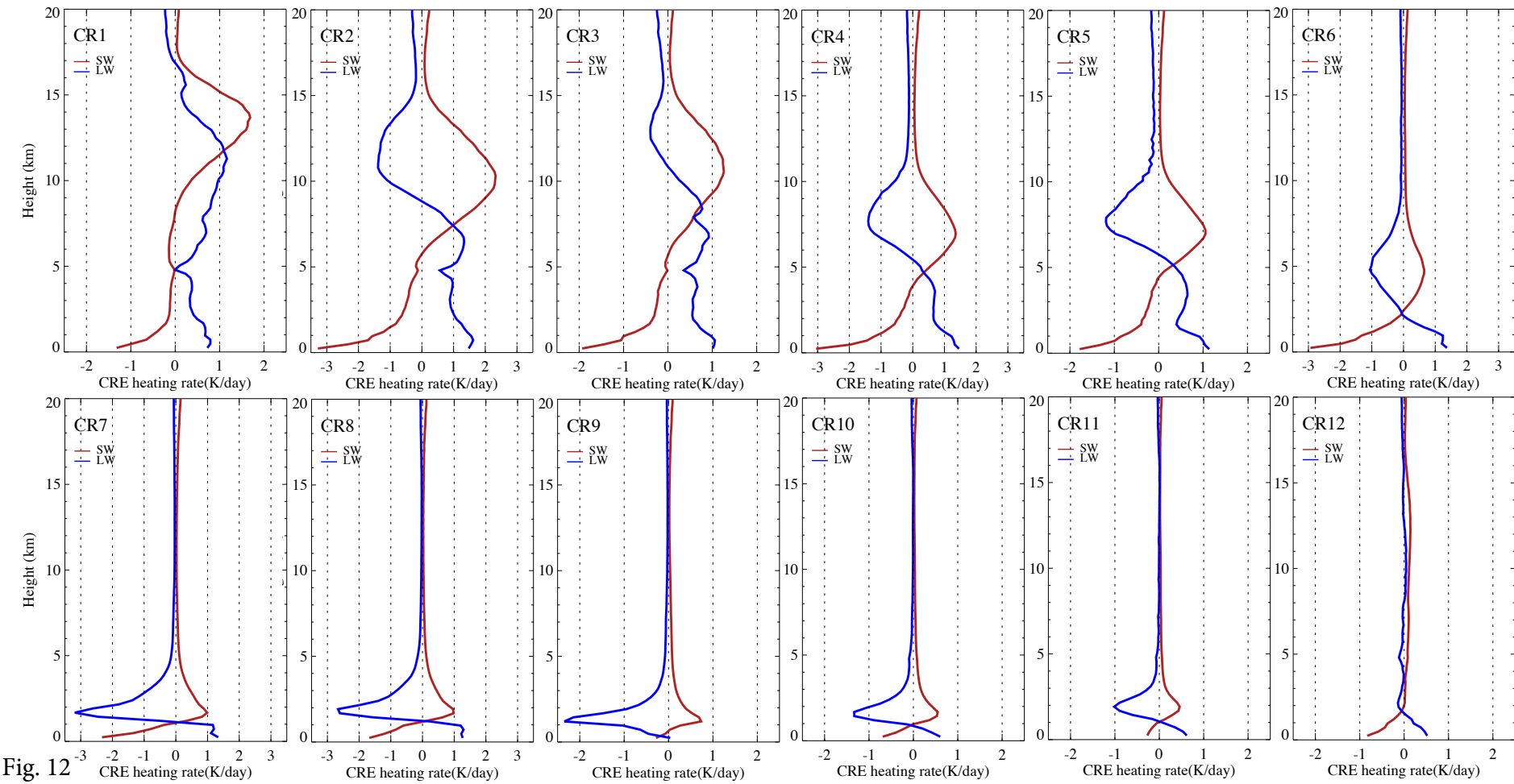


Figure 13

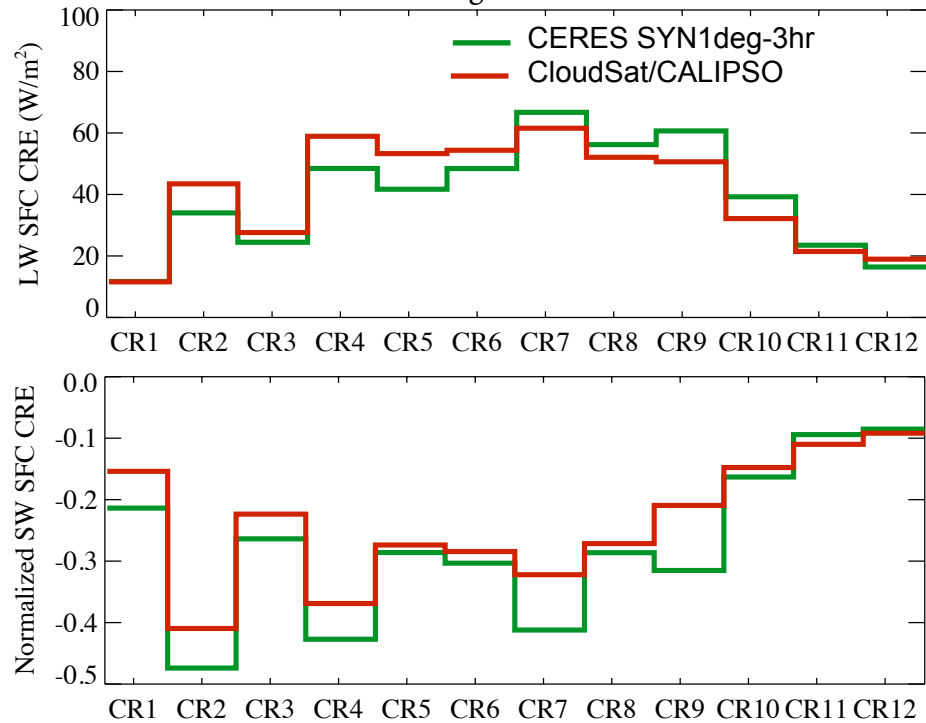


Figure 14

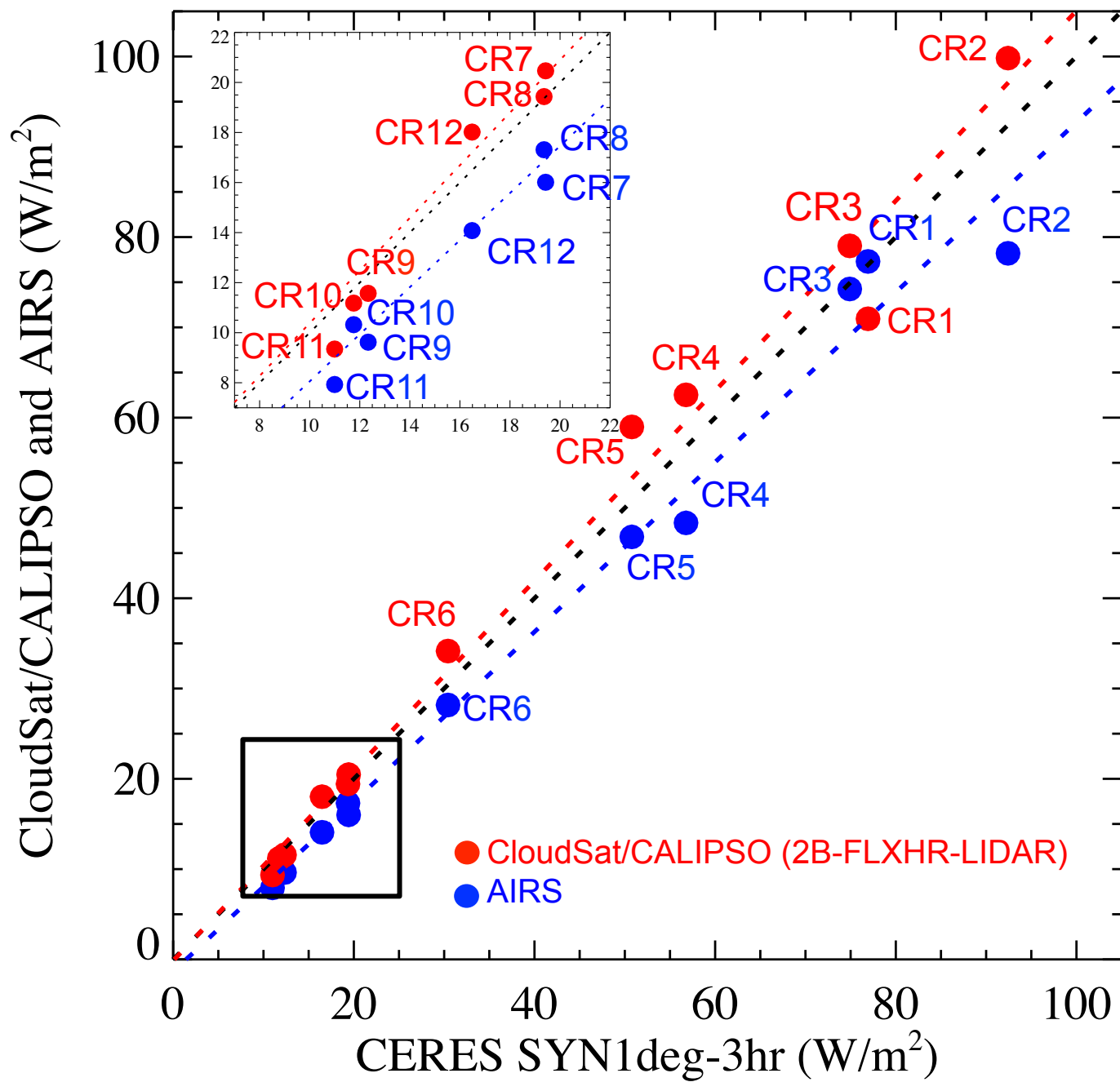


Figure 15

